



Contents lists available at ScienceDirect

## Journal of Volcanology and Geothermal Research

journal homepage: [www.elsevier.com/locate/jvolgeores](http://www.elsevier.com/locate/jvolgeores)

## Early Miocene Kirka–Phrigian Caldera, western Turkey (Eskişehir province), preliminary volcanology, age and geochemistry data

Ioan Seghedi <sup>a,\*</sup>, Cahit Helvacı <sup>b</sup><sup>a</sup> Institute of Geodynamics, Romanian Academy, Jean-Louis Calderon 19-21, Bucharest 020032, Romania<sup>b</sup> Dokuz Eylül Üniversitesi, Mühendislik Fakültesi, Jeoloji Mühendisliği Bölümü, TR-35160 Buca, İzmir, Turkey

## ARTICLE INFO

## Article history:

Received 16 June 2016

13 September 2016

Accepted 19 September 2016

Available online xxxx

## Keywords:

Kirka–Phrigian caldera

North-west Anatolia

Caldera collapse

Ignimbrites

Anatexys

## ABSTRACT

Large rhyolitic ignimbrite occurrences are closely connected to the Early Miocene initiation of extension in the central-western Anatolia crossing the Tavşanlı–Afyon zones. Field and laboratory data performed at the apex of the Eskişehir–Afyon–Isparta volcanic area allowed recognition of newly identified caldera structure, named here “Kirka–Phrigian caldera”. Transtensive/distensive tectonic stresses since 25 Ma ago resulted in the NNW–SSE elongation of the magma chamber and influenced the roughly elliptical shape of the subsided block (caldera floor). The caldera, which is roughly oval (24 km × 15 km) in shape, formed during a series of collapse events, starting at ~19 Ma, by the generation of a huge volume of extra- and intracaldera ignimbrites. Intracaldera post-collapse sedimentation and further volcanism at the northern edge (at ~18.6 Ma) were controlled through subsidence-related faults with generation of a series of volcanic structures (domes and lavas) showing a large compositional range. Enriched mantle components within the subcontinental lithospheric mantle began to melt via decompression melting during the initiation of extension. The heat resulting from the fractionation of ascending mantle melts produced the silicic compositions in large mushy crustal reservoirs; interaction of these melts with fertile crustal rocks further caused crustal anatexis and consequently two different compositions: Rhyolite-1 and Rhyolite-2. The eruptions of Kirka–Phrigian caldera-related ignimbrites were probably triggered by basaltic intrusion. Rock volumes and geochemical evidence suggest that silicic volcanic rocks come from a long-lived complex magma chamber system. After caldera generation there was a northern shift to small volume extra- and intra-caldera episodic rhyolitic, basaltic-trachy andesitic, trachytic and lamproitic volcanism, the latter being the youngest (16.2 Ma) indicating a more primitive magma input which originated in an enriched mantle lithosphere. The rock succession provides a direct picture of the state of the magmatic system at the time of eruptions that generated caldera and post-caldera structures and offers an excellent example of silicic magma generation and associated potassic and ultrapotassic intermediate–mafic rocks in a post-collisional extensional setting.

© 2016 Elsevier B.V. All rights reserved.

### 1. Introduction

The subject of this study is a newly identified caldera structure situated in the northernmost part of the Miocene Eskişehir–Afyon volcanic area (EAV) (e.g. Yağmurlu et al., 1997; Savaşçın and Oyman, 1998; Ersoy and Palmer, 2013) (Fig. 1). It has been known for a long time for its borate deposits, the largest in the world (e.g., İnan et al., 1973; Helvacı, 1977; Kistler and Helvacı, 1994; Helvacı and Alonso, 2000; Helvacı and Orti, 2004; Helvacı, 2005; García-Veigas and Helvacı, 2013; Helvacı et al., 2012). It was recognized that borates were formed in closed system lacustrine environments and were connected with thick volcano-sedimentary successions associated with marls, mudstones, limestones and sandstones; however the caldera system was not

revealed until now. Aydar et al. (1998) documented a caldera further south, acknowledged as the Köroğlu caldera (13 × 18 km in size).

In the geodynamic context of Anatolian geology, the surrounding area experienced ocean closure during the latest Cretaceous to Paleocene, resulting in the collision of the Anatolide–Tauride block in the east with the European margin, as marked by late Cretaceous and Paleocene high-pressure (HP) metamorphism of the Tavşanlı and Afyon zones (e.g., Okay et al., 1998; Okay, 2011). A detailed kinematic reconstruction of the Aegean region since 35 Ma suggests that during the Oligocene to Miocene clockwise rotation around poles in northern Greece argues for two stages of trench-perpendicular extension at 25–15 Ma and 15 Ma–recent. The opposite rotations of the eastern and western Aegean regions accommodated the Menderes and the Cycladic core complexes (e.g., Kissel et al., 2003; van Hinsbergen and Schmid, 2012) resulting in a large crustal deformation and associated magmatic activity of the eastern Anatolian side.

\* Corresponding author.

E-mail address: [seghedi@geodin.ro](mailto:seghedi@geodin.ro) (I. Seghedi).

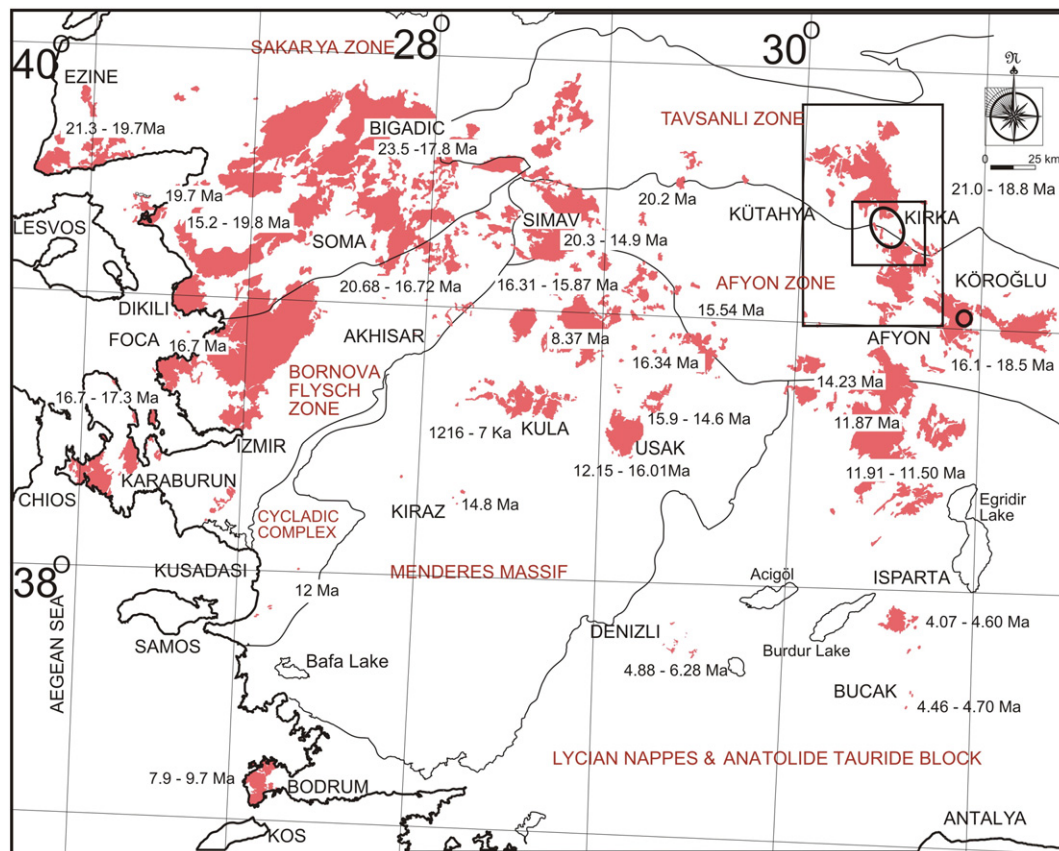


Fig. 1. Simplified map of western Anatolia (Turkey) modified from Fig. 1b of Prelević et al. (2015) and references therein, showing the major Miocene volcanic fields and their ages. The larger frame represents the distribution of volcanic deposits around the Kirka-Phrigian caldera and the inset frame represents the geological map of the caldera and its surroundings in Fig. 2.

The Miocene Eskişehir–Afyon volcanic area (EAV) was emplaced along a distinct ~N–S-trend graben-like system at the apex of the Isparta Angle, as result of the Early Miocene extension (e.g., Yağmurlu et al., 1997; Koçyiğit, 2005; Ersoy and Palmer, 2013). The volcanic activity began at Kirka during the Early Miocene, around 19 Ma, and continued to the south until ~12–10 Ma at Afyon (Floyd et al., 1998; Savaşçın and Oyman, 1998; Akal et al., 2013; Dilek and Altunkaynak, 2009, 2010; Prelević et al., 2012, 2015), finishing at Isparta at around 4 Ma and terminated at the Gölcük volcano at around 10 ka (Lefevre et al., 1983) and clearly implying a north to south migration of the volcanic activity. An increasing asthenospheric contribution from north to south has been suggested (Dilek and Altunkaynak, 2009; Prelević et al., 2012) (Fig. 1). This situation reflects a typical post-collisional geodynamic setting, implying local variations in the extent and nature of the interaction of a previously metasomatized lithospheric mantle and asthenospheric mantle triggered by its upwelling heat that could be explained by the presence of a slab tear (e.g. Prelević et al., 2015).

This paper is an introduction to the volcanology, petrology and eruptive history of one of the largest and yet unidentified collapse calderas of the Eskişehir–Afyon volcanics: the *Kirka-Phrigian caldera*, the name coming from the caldera area and its close surroundings (Figs. 1, 2). We attributed this name for two reasons: (1) the name of the main town inside the caldera, Kirka, and (2) during 8–6th century BC, the area was inhabited by one of the greatest civilizations in Anatolia, the Phrigian civilization, well known for their magnificent edifice excavations both on the volcanic deposits, especially ignimbrites, and on the limestone deposits, inside and/or outside the caldera margins.

This area was mapped by Gök et al. (1980) for borate. Their map helped us undertake a new reconnaissance study to re-evaluate the

volcanic facies distribution, reworked sedimentary deposition and hydrothermal activity. Another helpful fact was that the significant degrees of erosion and some tectonic disruption have resulted in a large number of outcrops showing vertical sections, especially in the intracaldera sequences. Several boreholes also have been crucial for understanding the depth of the caldera floor, hidden lithology and volume estimation.

## 2. Geological, volcanological and petrographic data

### 2.1. Pre-caldera basement rocks

The caldera seals the basement between the Tavşanlı and Afyon Zones. The Tavşanlı Zone is represented by Palaeozoic metamorphic rocks, a Mesozoic ophiolite complex and Eocene fossiliferous limestone (Okay and Satır, 2006; Okay, 2011). The Paleozoic and Mesozoic units of the Afyon Zone, south of the Kirka area, have been dated paleontologically despite their low-grade metamorphism (Göncüoğlu et al., 1992). The Paleozoic sequence starts with clastic metasediments and is composed of quartzite, phyllite and quartz phyllite intercalations and finally by thick dolomitic platform metacarbonates. The Mesozoic sequence consists of thin-bedded marble and thick-bedded massive dolomitic marble up to early Maastrichtian. It is succeeded by upper Maastrichtian–Lower Paleocene olistostromal wildflysch with limestone, serpentinite, radiolarites and mafic ultrabasic volcanic rocks and blueschist blocks (Özcan et al., 1988; Göncüoğlu et al., 1992) that have been metamorphosed in greenschist facies. Parts of the ophiolitic rocks were metamorphosed under high pressure and low temperature resulting in lawsonite and glaucophane-bearing schists (Okay et al.,

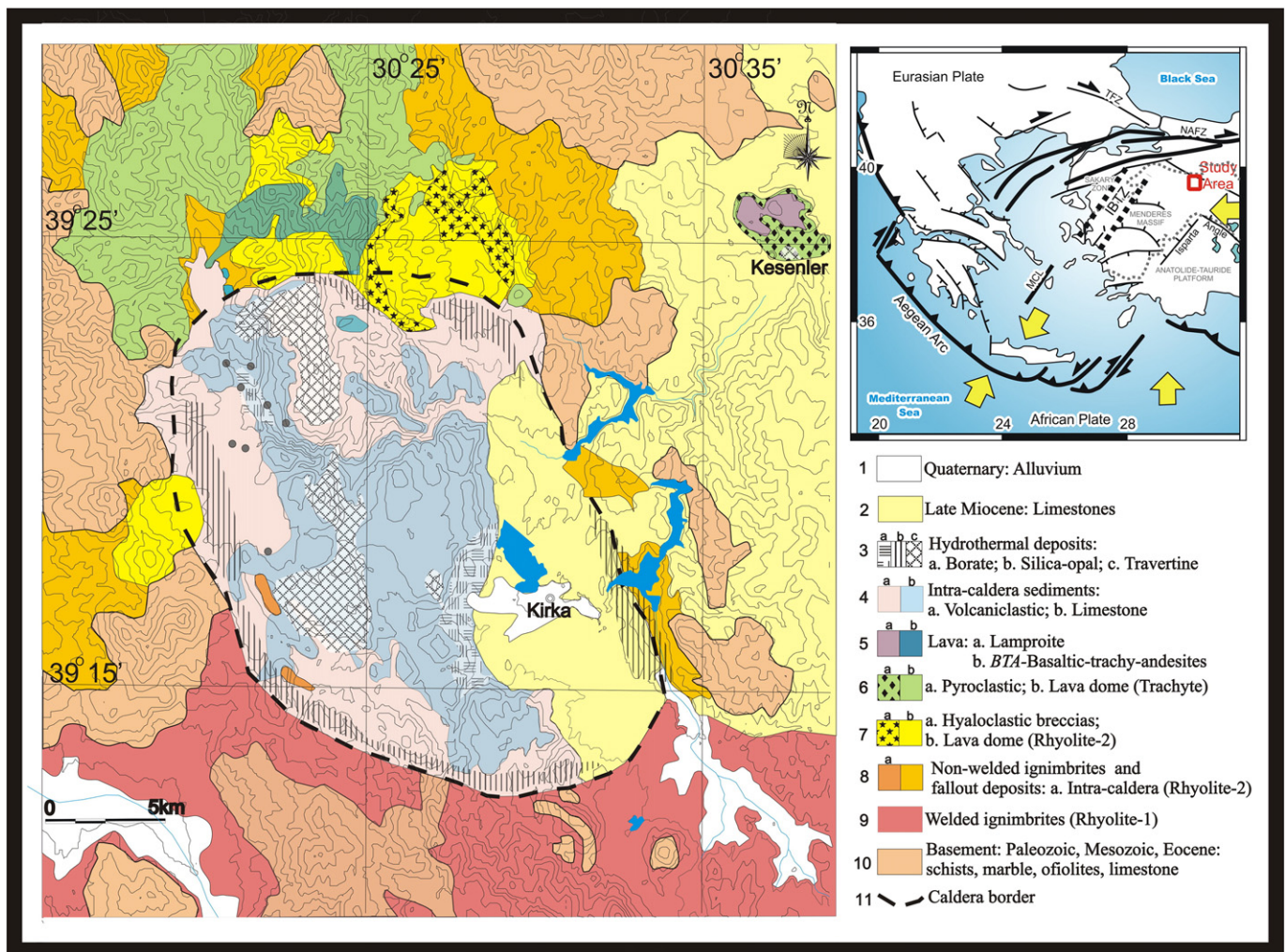


**Fig. 2.** Geological map of the Kirka-Phrigian caldera displaying also the 50m level curves. The inset is showing the study area at the northern edge of the Isparta angle in the context of simplified tectonic map of the eastern Mediterranean. The locations of the drillings are marked on the map as grey dots. The individual boreholes are labelled in the bottom left-hand panel of Figure 6.

1998). All of these units are unconformably covered by un-metamorphosed Lower Eocene shallow water sediments consisting of siltstones, marly limestones and limestones, around the Kirka area (Özcan et al., 1988).

## 2.2. Caldera structure recognition

The way in which the elliptical shape of the caldera has been recognized includes (see Fig. 2):

- (1) Recognition of Middle-Late Miocene deep level of erosion (in its eastern part) that was followed by a new regional limestone deposition during Late Miocene, enhanced during Late Miocene-Quaternary times, makes it challenging to recognize the eastern topographic rim of the caldera;
- (2) Rare “lag-breccia” associated with welded ignimbrites (showing outward-dipping bedding) all along the southern margin shows a discordant contact with Miocene intra-caldera limestones (with inward dipping bedding); extra-caldera ignimbrites and associated fall deposits are characteristically spread all along the northern rim toward the north up to a 30 km distance;
- (3) The occurrence of secondary silica deposition and sub-vertical silica (opal) veining all along the inside of the caldera margin

suggests reactivation of the ring faults following collapse and the nearness of its structural margin;

- (4) A sequence of lava domes of continuous changeable composition: rhyolite, trachyte as domes and basaltic-trachy-andesites, or basalts and lamproite, as sill/lava flow (in boreholes) has been documented all along the northern margin rim that suggests their generation in a post-caldera stage, being facilitated by the ring fault system;
- (5) The generation of boron minerals and large travertine deposits, are exclusively inside the caldera walls, mainly along ~N-S trending faults, suggesting an important tectonic reactivation in the late post-caldera stage, post-dating a large basin generated by the collapse and further filled with pyroclastic deposits or various sediments (as terrigenous volcanoclastic and precipitated limestones).

## 2.3. Volcanic rocks associated with caldera formation

The most extensive volcanic deposits are rhyolitic ignimbrites distributed all around the caldera, but rarely observed inside. According to their position in respect to the caldera, but also considering welded



**Fig. 3.** Volcanology field description: 3a – Thick basal sequence of welded ignimbrites seen from the south, showing vertical columnar jointing; inlet is showing a detail of a rheomorphic flow deposit with dark glassy fiamme; 3b – deposit of lag-breccia at the southern margin of the caldera; 3c – pyroclastic fall and surge deposits at the top of the basal flow followed next by thick pyroclastic deposit; 3d – thick accretionary lapilli deposit at the south-eastern margin of the caldera; the size of one rounded lapilli may reach 6 cm in diameter; 3e – slightly welded ignimbrite at the site of the palace of Phrigian King Midas, carved in such ignimbrites; 3f – thick succession of fall-out deposits outside the caldera in the north-western part; 3g – large rhyolite domes surrounded by hyaloclastic breccia (see inlet); 3h – section in the outcrop in the Kesenler volcano showing a succession of trachytic fall-out lapilli to fine tuffs (see inlet) and in the top a dark lamproite lava.

and non-welded facies, two main types of ignimbrites were recognized, extra-caldera and intra-caldera deposits (Fig. 3).

### 2.3.1. Extra-caldera ignimbrites

There are of two types of extracaldera ignimbrites: (1) welded and (2) slightly or non-welded.

#### 2.3.1.1. The welded ignimbrites generated a thick pyroclastic flow unit.

Transition to slightly to moderately welded ignimbrites suggests several flow unit packages (no detailed study was done). The most well-preserved outflow pyroclastic deposits are spread toward the south (e.g. Keller and Villari, 1972; Floyd et al., 1998; Figs. 2, 3a) and here considered as Rhyolite-1, based on their geochemical and isotopic compositions. The base of this volcanic sequence is exposed at the southern structural margin of the caldera and is sometimes associated with a lag breccia (Fig. 3b). There is an estimated exposed thickness of ~300 m, consisting of a thick basal flow unit of ~200 m and 2–3 m following minor flow units (e.g. Keller and Villari, 1972). The welded ignimbrite deposits are infrequently associated with surge and fall deposits (Fig. 3c). Dominantly, a single flow unit shows a columnar vertical jointing, assumed to result from rheomorphic flow deposition (Lipman, 2000). The individual thickness of the minor flow units are 10–50 m with a poorly defined contact between units, except where fall or surge deposits are present. The ignimbrites occur as extensive continuous sheets, however their thickness is increasing in pre-caldera valley morphologies and decreasing to the south up to 35 km and covering a surface of ~300 km<sup>2</sup>, where they split into thinner flows. Close to the caldera margin, the deposits show abundant dark glassy fiamme (10–22%), suggesting a high degree of flattening and welding that diminishes further away (Fig. 3a inset). Typically the ignimbrite is a vitric-crystal tuff with lithic and pumice that are both flattened/welded and unwelded. The pumice clasts show a rather similar proportion from the caldera walls toward the exterior; however a centrifugal diminishing of their size can be envisaged (from dm to cm). Thickness variation also strongly depends on the pre-existing topography that shows uneven morphology of the basement exposure all along the caldera margin (Fig. 2). Thicker units suggest the presence of a series of cooling units; however the absence of a sharp and erosive base in-between suggests a continuous process of eruption. Since in most cases internal depositional boundaries are missing, in the case of the basal flow it may be considered that progressive aggradation from a maintained pyroclastic flow was dominant over short-lived flows (Freundt et al., 2000)

2.3.1.2. Slightly or non-welded ignimbrite facies is well represented inside and toward the east, north and west outside of the caldera where it is always associated with thicker fall-out deposits (up to 50 m). They were attributed to Rhyolite-2, based on their geochemistry. In the south-eastern part along the caldera margin, thick (40–60 m) accretionary lapilli fall-out deposits were found (Fig. 3d). The ignimbrites' thickness decreases toward the north up to 35 km, covering a surface of ~1000 km<sup>2</sup>, according to the Geological map of Turkey, sheet Ankara, scale 1:500,000.

### 2.3.2. Intracaldera ignimbrites

The intra-caldera ignimbrite shows a smaller amount of outcrops toward the southern part (Fig. 2). The deposits are slightly welded, and are similar to the ignimbrites distributed all around the caldera walls toward east, west and north (Fig. 3e). According to borehole data, they also occur inside the caldera depression from 1200 to 1000 m depths and up to several hundreds of meters in thickness (e.g. García-Veigas and Helvacı, 2013). These ignimbrites are also associated with a thick succession of fall-out deposits, up to tens of meters in thickness (Fig. 3f).

Compositionally, both extra and intra-caldera ignimbrites show phenocryst fractions ranging 15–30% (20–15% quartz, 25–15% K-feldspar, 10–5% plagioclase, 5–8% biotite) in an 85–70% vitric matrix, mostly

devitrified (Fig. 4a, b). The lithic fraction is dominated by fragments of crypto-crystalline texture. Both facies are rhyolitic in composition, but since they display quite different geochemical compositions (see Section 4) they have been termed, as mentioned, Rhyolite-1 and Rhyolite-2. As a characteristic, garnet xenocrysts are frequently present in the Rhyolite-1 ignimbrites (e.g. Keller and Villari, 1972).

### 2.4. Post-caldera (post-collapse) volcanic rocks

In the northern segment of the caldera, the topographic border of the subsided block is almost completely hidden by younger volcanic rocks (Fig. 1) and recent erosional processes, so the extent of the collapse margin is not discernible, only inferred. The post-collapse volcanic rocks are represented by various kinds of volcanic forms dominated by domes that according to the field relationships, attest to the rhyolite as first-generated, then by trachytic domes that shield the rhyolitic ones. On top of the mentioned domes, along and outside caldera-border faults, a series of lavas occur, with basaltic-trachy-andesites and lamproite composition, showing one significant and several minor centers (Fig. 2). All the rock names are according to their petrochemistry.

- The *rhyolite domes*. There are at least three important large rhyolite domes. The north-easternmost one has a circular shape, up to 8 km in diameter and is surrounded by hyalo-breccia envelope showing cm-dm size (Fig. 3g). It is strongly eroded along a present-day valley that may indicate a former caldera fault collapse system (Fig. 2). The central rhyolite dome structure shows an N-S elongation (9 × 6 km) and looks to be in contact with the eastern dome; however its breccia envelope is missing. A third western rhyolite dome (5 × 3 km) is situated at the caldera margin between two large areas of exposed basement. The rocks forming the domes generally show a fluidal texture dominated by a glassy groundmass that ranges from 40 to 60% with similar crystal content as the ignimbrites (25–10% quartz, 20–10% K-feldspar, 10–5% plagioclase, 8–4% biotite). Fewer crystals characterize the hyalo-breccia at the margins of the eastern dome. They correspond geochemically to Rhyolite-2.
- The *trachyte domes* largely developed as two main structures elongated N-S at the northern margin of the caldera (10–15 × 7 km) and cover the caldera-related ignimbrites and associated deposits, the rhyolite domes, as well the basement deposits. Rarely hyalo-breccias occur at their margins. The rocks are largely porphyritic and have a series of phenocrysts: 5% biotite, 5% amphibole, 30% K-feldspar, 20% plagioclase feldspar in a 35–40% groundmass, sometimes devitrified (Fig. 4c).
- The *basaltic-trachy-andesites (BTA)* occur as several lava flows at the northern margin. Their composition includes 10% olivine, 10% clinopyroxene phenocrysts and ~80% matrix composed of plagioclase, pyroxene and opaque minerals (Fig. 4d).
- The *basalts* have been found only in borehole 2009/1, m. 955.8 (Fig. 2) as a sill rather than lava flow. Its composition includes 10% olivine, 8% clinopyroxene and 12% plagioclase phenocrysts in an ~70% very fine groundmass composed of plagioclase and opaque minerals.
- The *lamproites* form lava flows and are composed of 24–28% olivine, 22–26% clinopyroxene, 4–6% phlogopite phenocrysts and ~40–52% dominantly feldspathic matrix (Fig. 4f).
- The *trachytes* have been also found as an extra-caldera small dimension volcanic structure (~2.2 km in diameter) at Kesenler town, 8 km NE from the caldera border (Fig. 2), we named it the *Kesenler volcanic structure*. The small edifice is strongly eroded and characterized from the base to the top by a succession of trachytic fall-out lapilli to fine tuffs (Fig. 3h), followed by a trachytic dome-collapse breccia, another sequence of fall and flow pyroclastic deposits, all shielded by lamproite lavas that show an oriented flow toward the NNE (Figs. 1, 3h, 4f). Taking

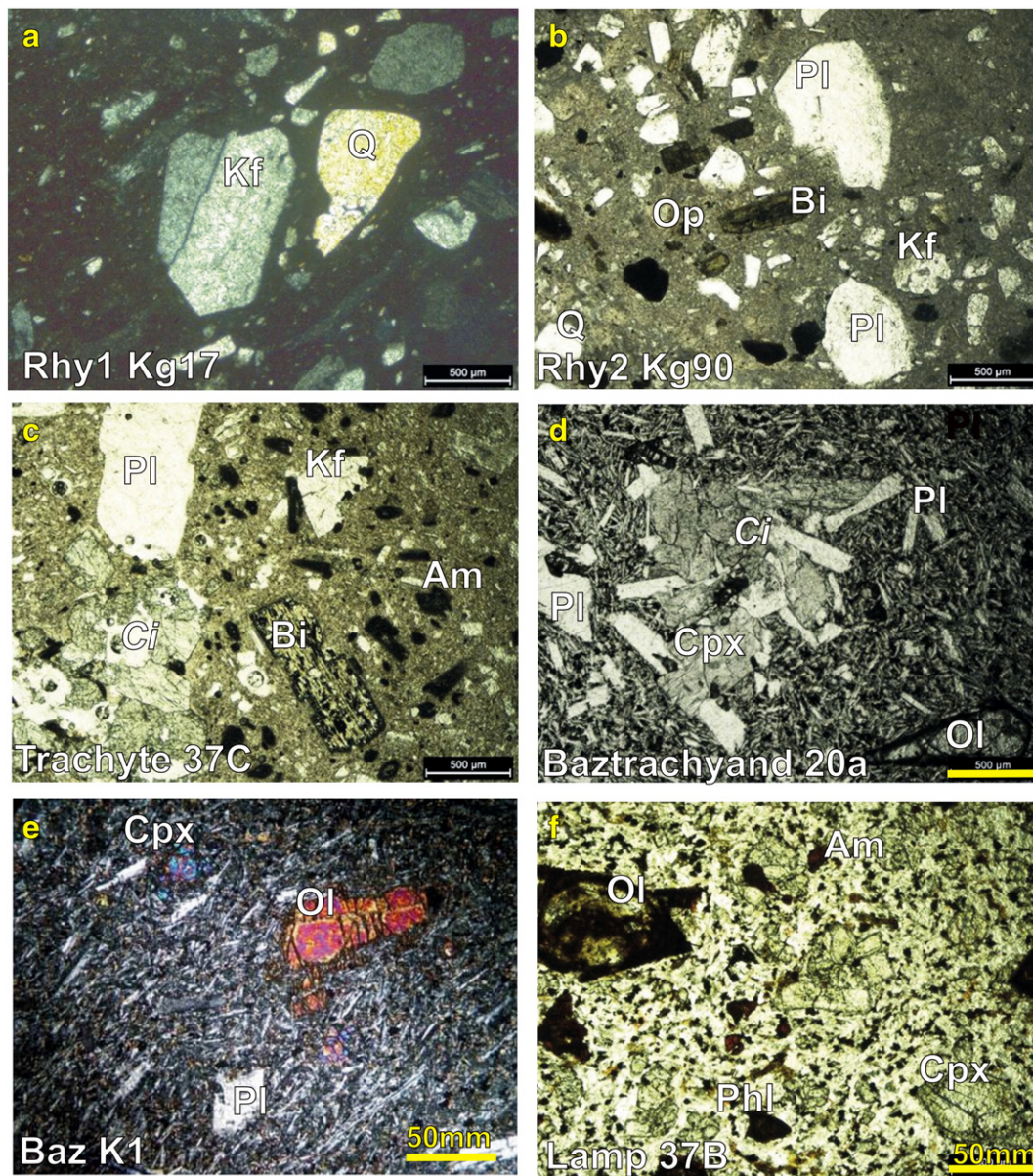


**Fig. 4.** Microscope view of selected samples (see description in the text). a. Sample KG-111, Rhyolite-1 ignimbrite, note the irregular margins of the large crystals (Pl – plagioclase, Kf – K-feldspar, Q – quartz); b. sample KG-90, Rhyolite-2 ignimbrite, note the presence of irregular margins of plagioclase (Pl), biotite (Bi), quartz (Q) and opaque minerals (Op); c. sample 37C, trachyte lava-dome, note the presence of the irregular shape of cognate inclusion (Ci) as well as Pl – plagioclase, Kf – K-feldspar, Bi – biotite and Am – amphibole; d. sample 20a, basaltic-trachyte-andesite lava, note the irregular shape of cognate inclusion (Ci) comprising clinopyroxene (Cpx) and plagioclase (Pl) also Pl – plagioclase and Ol – olivine phenocrysts; e. sample K1, sill/lava basalt, note the slightly oriented texture of fine grained Pl – plagioclase and Op – opaque-dominated groundmass and Pl, Ol and Cpx phenocrysts; f. sample 37B, lamproite, showing small phenocrysts of Ol – olivine, Cpx – clinopyroxene, Phl – phlogopite and Am – amphibole in a feldspathic groundmass.

into account the well-developed travertine deposits east of Kesenler town, it is probable that this corresponds to the central vent area of this small, eroded volcano. The northern slopes of both trachytic tuff deposits and lamproitic lava flows are covered discordantly by Late Miocene limestones.

## 2.5. Post-caldera (basin-filling) deposits

The information about post-intra-caldera deposits is based on outcrop exposures and boreholes. Within the caldera, starting from its upper margins, debris flow deposits are dominant with various

erosional contacts. Several units of precipitated limestone have been found, mostly intercalated with secondary, epiclastic deposits.

### 2.5.1. Outcropping intra-caldera sedimentary deposits

The sedimentary record, over 150 m thick in some places, is exposed by valley-streams incision in the northern part (Fig. 2). The observed deposits are either detrital (volcaniclastic-epiclastic) or precipitated (limestones or dolomites), randomly alternating. The detrital deposits consist of horizontal discontinuous-bedded sandstone, low-angle trough or scour-fill cross-bedded sandstone or breccias, massive poorly-sorted sandstones and conglomerates, suggesting lahar and fluvial-

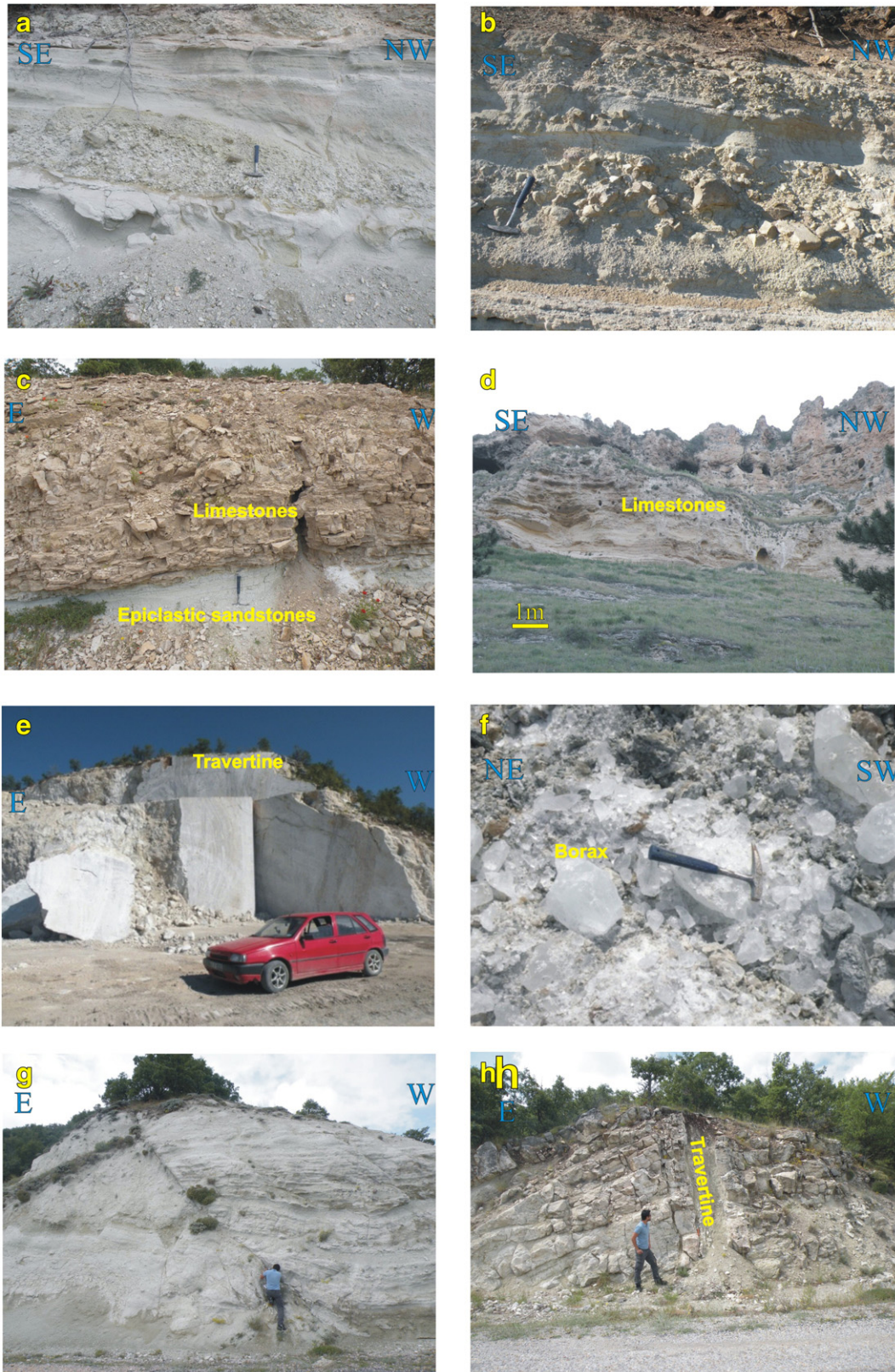


**Fig. 5.** Intra-caldera-sedimentary deposits and faults (see description in the text): a. low-angle trough or scour-fill cross-bedded breccias in the north-western side of the caldera interior; b. massive poorly sorted sandstone and conglomerate succession close to the north-western side of the caldera; c. stratified limestones and dolomites covering an epiclastic sandstone deposit in the eroded central part of the caldera; d. succession of stratified limestones showing Phrigian historical excavations in the southern part of the caldera interior; e. quarried large vertical travertine vein in the south western part of the caldera interior; f. large crystals of borax in the main quarry exploitation of ETIBANK Mine Company; g. north-south directed normal faults cutting epiclastic deposits in the north-western part of the caldera interior; h. N-S oriented vertical travertine vein cutting epiclastic deposits in the north-western part of the caldera interior.

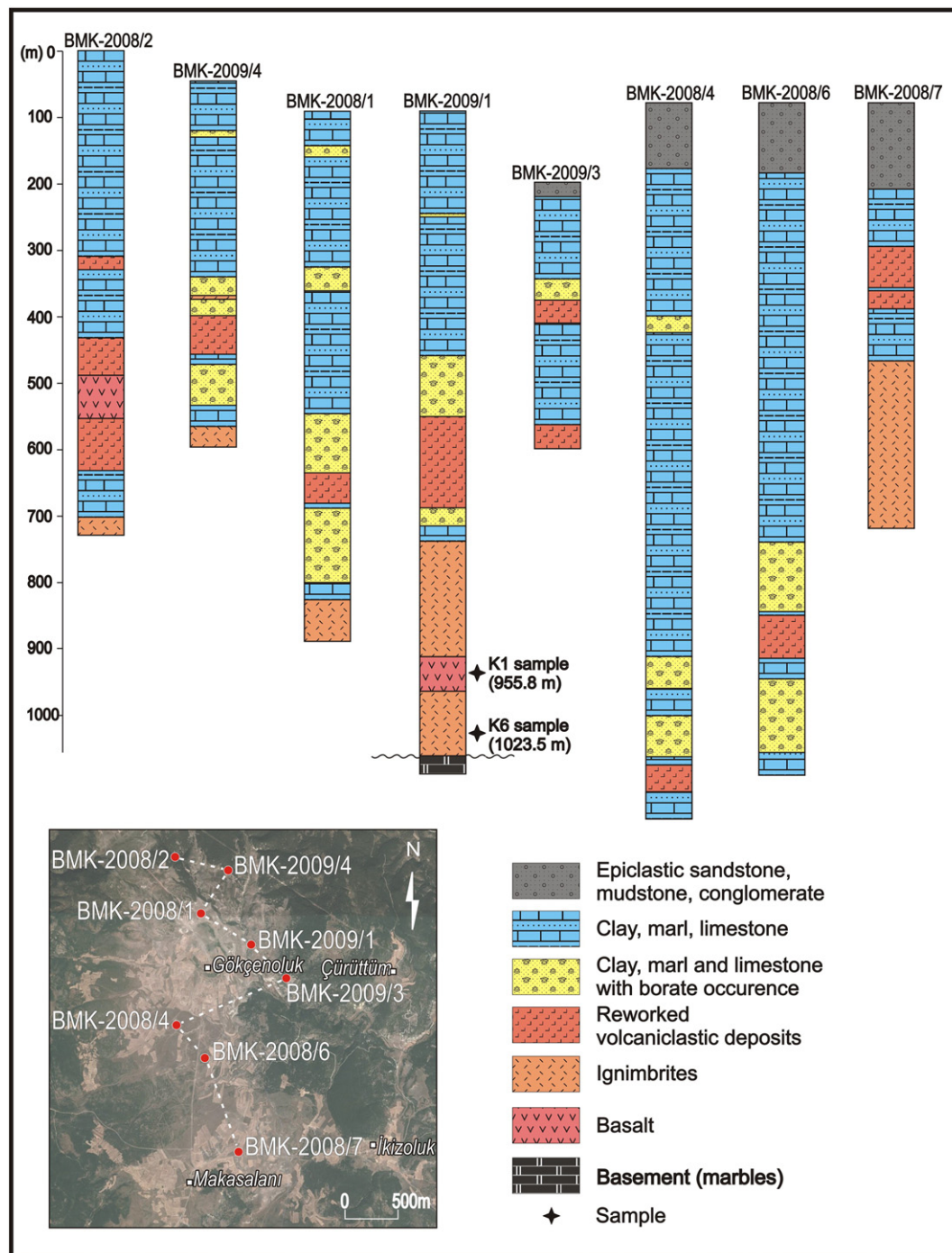


**Fig. 6.** The lithology of the drilling done by ETİBANK Mine Company for borate deposits in the Gökenoluk area (see text for explanation). The location of the drillings are shown in a Google map in the bottom left-hand panel and also marked on the figure 2. The figure exposes the samples location used for age determinations and geochemistry from the drillhole BMK-2009/1.

channel deposition (Fig. 5a, b). The upper sequences are better exposed and are cm to 20 m thick beds showing a fine- to coarse-grained matrix composed mostly of rhyolitic detritus, as quartz, plagioclase, K-feldspar, biotite, glass shards and rounded pumice. The larger massive clasts are either rhyolite or trachyte. The massive rocks (domes) have been also an important source. The limestones and dolomites are ascribed to Middle Miocene and are cm-dm-size stratified (Fig. 5c, d). They also were described as stromatolitic or cherty (Inan et al., 1973; Helvacı, 1977; Helvacı and Orti, 2004; García-Veigas and Helvacı, 2013).

#### 2.5.2. Drilling data

A series of 8 boreholes were drilled in the northeastern area of the caldera for boron mineralization purposes, by (Fig. 2). Our simplified lithology of the borehole data is given in Fig. 6 (with the permission of ETİBANK Mine Company). Only the BMK-2009-1 reached the basement at ~1100 m. The ignimbrites and volcaniclastic deposits are dominant from the bottom up to 400 m depth, overlain by sequences of clay, marls and limestones, attributed to the Middle Miocene (Inan et al., 1973; Helvacı, 1977) in the northern sequence between BMK-2008-2

**Table 1**  
Whole-rock major, trace element, Sr-Nd isotope analyses and location of representative samples from Kirka-Phrigian caldera and Kesenler volcano.

Sample	KG-37B	K1	K1-1	K4-3	K4	KG-94	KG-20A	KG-20B	KG-100A	KG-37A	KG-37C	KG-1	KG-17A	KG-111	K6	KG-91	KG-62	KG-50B	KG-90	KG-104
Rock type	L	B	B	BTA	BTA	BTA	BTA	TA	TD	TD	TD	Rhy1	Rhy1	Rhy1	Rhy2	Rhy2	Rhy2	Rhy2	Rhy2	Rhy2
SiO <sub>2</sub>	51.06	47.19	47.90	51.58	52.31	53.31	52.13	56.33	62.74	66.29	63.29	72.02	75.74	73.02	68.82	69.49	71.05	68.66	72.84	74.72
Al <sub>2</sub> O <sub>3</sub>	14.69	17.28	17.22	16.54	16.68	16.39	15.69	16.87	15.52	15.2	15.06	13.07	12.2	12.87	14.34	14.09	13.13	14.55	11.87	12.95
Fe <sub>2</sub> O <sub>3</sub>	6.7	8.72	8.34	6.35	6.68	6.39	7.29	5.93	4.79	3.73	4.61	0.55	0.83	2.67	2.98	3.5	0.85	3.26	2.89	1.27
MgO	6.06	5.98	6.70	3.60	4.87	4.47	6.48	3.98	1.98	1.36	2.31	0.42	0.07	0.1	1.03	0.7	0.17	0.93	0.77	0.09
CaO	7.63	10.70	10.36	9.25	8.57	7.64	7.67	5.51	4.18	3.16	4.62	0.96	0.81	0.82	2.77	2.18	0.98	2.82	2.31	1.29
Na <sub>2</sub> O	2.54	3.27	3.20	3.10	3.09	3.04	2.96	3.31	3.43	3.52	3.19	2.13	3.18	3.18	2.89	3.13	1.83	3.46	2.5	3.43
K <sub>2</sub> O	4.99	0.68	0.57	2.96	2.86	3.09	2.87	4.65	4.32	4.54	4.02	5.53	5	5.27	5.00	4.55	6.51	4.23	3.45	4.82
TiO <sub>2</sub>	1.33	1.32	1.31	0.96	1.01	0.95	0.93	0.84	0.65	0.51	0.64	0.04	0.04	0.04	0.65	0.51	0.1	0.45	0.42	0.15
P <sub>2</sub> O <sub>5</sub>	0.6	0.21	0.21	0.46	0.45	0.48	0.43	0.51	0.38	0.16	0.17	0.01	0.02	0.03	0.35	0.16	0.04	0.15	0.13	0.03
MnO	0.12	0.13	0.15	0.14	0.12	0.1	0.13	0.1	0.1	0.07	0.09	0.04	0.02	0.03	0.03	0.03	0.08	0.06	0.02	0.02
LOI	3.8	4.2	3.7	4.6	2.9	2.7	3	2.1	1.4	1.2	1.6	5	1.9	1.8	0.8	1.4	5.1	1.1	2.5	1
Total	99.58	99.74	99.72	99.65	99.59	98.59	99.67	99.61	99.67	99.73	99.61	99.84	99.84	99.85	99.69	99.74	99.79	99.66	99.73	99.77
Ni	87	41	48	114	119	71	120	33	4	5	9	5	5	4	26	6	5	6	5	4
Sc	21	28	28	21	21	17	20	20	11	8	13	3	3	4	7	4	4	7	5	3
Ba	1263	238	214	1163	1376	1191	1151	1381	1083	873	1510	62	63	30	1301	845	631	1343	907	825
Co	39	40.1	79.3	49.7	36.2	32.6	37.6	19.3	20.6	21.9	47.8	28.3	52.8	30.1	22.2	31.2	54.3	41.4	23.9	38.3
Ga	15.9	14.7	13.6	13.9	14.8	16.9	15.3	18	19	16.7	17.3	17.6	16.4	16.3	14.2	15	15.1	16.5	13.8	15
Hf	10.1	3.0	2.8	4.6	4.7	6.1	4.9	5	6.4	5.6	4.6	3.7	3.9	3.3	5.9	5.3	3.2	4.7	3.9	2.7
Nb	26.7	6.1	6.4	14.0	13.9	23.3	13.9	17.4	16.1	17.2	16.3	39.2	34.8	33.9	19.4	15.3	22.6	15.9	12.7	15.7
Rb	169.8	35.4	25.4	106.5	96.8	148.8	101.3	175.9	141.5	164.1	138.1	479.3	375.7	391.3	213.2	172.4	238.3	153.9	157.6	189.6
Sr	798.2	453.4	458.7	598.5	596.3	652.7	546.2	604.9	490.9	315.5	482	38.2	23.3	23.5	419.0	256.8	103.8	331.9	284.6	128.8
Ta	1.5	0.4	0.4	0.7	1.2	1.4	0.9	1	1.2	1.5	1.4	5.2	5.2	4.7	1.8	1.4	2.8	1.4	1.2	2
Th	18.2	2.4	2.4	12.3	12.4	22.6	11.5	15.6	15.6	24.3	20.4	37.3	35	33.9	22.6	23	23.8	23.9	16	23.9
U	4.9	1.0	0.8	3.4	3.5	6	3.1	3.5	5.2	7.9	6.5	20.7	16.9	10.8	5.2	6.5	12.5	6.7	5.2	5.6
V	166	199	168	149	187	131	150	173	77	62	99	10	5	5	77	43	5	59	66	13
Zr	396.1	128.3	114.4	177.1	192.0	261.4	182.6	217.9	246	195.4	174.8	79	65.2	66.3	227.3	203.6	79.2	157.2	145.9	71.9
Y	21.1	22.4	21.5	21.5	23.5	22	22.1	27.5	30.3	22.2	23.6	68.9	40.4	56.2	22.4	21.5	19.9	20	23	14.1
La	68.2	13.3	11.1	36.5	43.8	57.8	35.2	44.7	39.8	42.4	38.5	17.1	15.6	15.7	40.5	40.1	29.6	40.9	34.2	34.1
Ce	132.9	28.3	26.0	73.2	81.9	107.3	68.6	82.3	75.5	73.3	66.5	34.7	31.2	40.9	76.0	66	51.8	72.7	59.2	56.6
Pr	15.38	3.45	3.25	8.15	9.03	12	7.87	9.91	8.87	7.78	7.55	4.7	4.07	4.01	7.72	7.24	5.17	7.81	6.18	5.78
Nd	57.2	14.7	13.6	29.6	35.0	44.9	30.9	38	34.2	25.3	27.3	16.8	15.4	15	27.5	25.1	17.5	25.5	19.9	17.3
Sm	9.03	3.55	3.26	5.92	6.41	7.73	6	7.38	6.72	5.01	5.24	5.87	4.83	4.75	4.77	4.6	3.31	4.66	3.89	3.18
Eu	2.13	1.16	1.10	1.52	1.63	1.73	1.43	1.57	0.86	1.09	0.18	0.16	0.15	1.02	0.85	0.43	0.86	0.75	0.49	
Gd	6.85	4.04	3.85	5.12	5.72	6.35	5.16	6.8	6.25	4.28	4.8	7.26	5.32	5.85	4.61	4.1	3.11	4.41	3.54	2.79
Tb	0.83	0.66	0.65	0.73	0.82	0.79	0.74	0.87	0.9	0.65	0.71	1.41	1.01	1.13	0.72	0.6	0.51	0.62	0.55	0.41
Dy	4.59	3.95	3.81	4.48	4.60	4.28	3.93	5.26	5.22	3.6	4.13	9.97	6.72	7.97	4.16	3.95	2.83	3.56	2.81	2.39
Ho	0.73	0.84	0.81	0.81	0.92	0.86	0.78	0.99	1.05	0.76	0.84	2.11	1.36	1.65	0.86	0.68	0.66	0.72	0.71	0.45
Er	2.05	2.35	2.32	2.26	2.72	1.99	2.2	2.57	2.91	2.19	2.25	6.45	4.18	5.43	2.23	2.12	1.9	1.98	1.6	1.13
Tm	0.29	0.36	0.34	0.36	0.37	0.34	0.31	0.36	0.43	0.34	0.34	1.14	0.68	0.87	0.34	0.33	0.28	0.31	0.29	0.18
Yb	1.85	2.23	2.04	2.28	2.55	2	2.13	2.08	2.71	2.15	2.45	7.81	4.88	5.77	2.06	2.32	1.93	1.89	1.54	1.21
Lu	0.28	0.34	0.35	0.33	0.37	0.28	0.34	0.34	0.4	0.33	0.37	1.23	0.71	0.93	0.33	0.36	0.32	0.28	0.29	0.16
Cu	16.6	15.0	14.9	24.7	28.1	23.5	20.6	62	0.5	2.4	5.3	0.7	0.5	0.7	11.1	1.3	0.2	2.3	1.5	0.6
Pb	2	2.5	2.5	3.5	5.7	5.4	5.4	17.9	2.3	3.7	5.7	13.5	5.4	12.1	8.6	5.7	1.9	5.8	3.3	3
Zn	34	48	56	59	45	42	40	32	34	27	28	5	12	44	24	14	1	26	17	14
<sup>87</sup> Sr/ <sup>86</sup> Sr	0.7067	0.7057				0.7079	0.7077	0.7077	0.7091	0.7089	0.7084	0.7184		0.7211	0.7095	0.7094		0.7089		
<sup>143</sup> Nd/ <sup>144</sup> Nd	0.5125	0.5128				0.5124	0.5125	0.5125	0.5124	0.5124	0.5124	0.5123		0.5123	0.5124	0.5124		0.5124		
x	30.648	30.392	30.392	30.424	30.424	30.354	30.424	30.424	30.346	30.648	30.648	30.405	30.422	30.470	30.392	30.337	30.568	30.528	30.348	30.504
y	39.418	39.386	39.386	39.380	39.380	39.401	39.380	39.380	39.348	39.418	39.418	39.252	39.302	39.223	30.386	39.406	39.324	39.329	39.397	39.401

Abbreviations: L – lamproite; B – basalt; BTA – basaltic-trachy-andesite; TA – trachyandesite; TD – trachydacite; Rhy1 – Rhyolite-1; Rhy2 – Rhyolite-2.

and BMK-2009-3 (Fig. 6). Southward the lithology of BMK-2008-4 and 6 is dominated by the clay, marls and limestone sequence, suggesting an association of distal fluvial and carbonate precipitation (e.g., McLane, 1995), also thinner volcanoclastic deposits at the bottom and most likely a deeper caldera floor. The southernmost BMK-2008-7 shows a similar lithology with the northern boreholes with an upper sequence of epiclastic deposits already documented at Section 2.5.1.

### 2.6. Deposits related to hydrothermal activity (borates, silica, and travertine)

Post-caldera activity favored important sedimentation in the basin, as documented by the presence of various reworked volcanoclastic deposits, rare interbedded lavas or sills, late-stage hydrothermal activity with secondary silica and dominant deposition of B-minerals and by crosscutting travertines (Fig. 5e, f). The secondary silica deposition and sub-vertical silica (opal) veining were found all along the inside of the caldera margin (Fig. 2). The B-mineralization is situated along the western interior of the caldera, suggesting a N-S trending fault system, most probably an important tectonic reactivation during post-caldera stage. The hydrothermal activity enriched in B, and also variably in Li, S, Sr and As, precipitated various B-minerals, especially the fine-grained sedimentary sequence of the caldera basin. The Early Miocene acidic volcanism with vast ignimbrite occurrences and high volume of elements associated with B-mineralization is considered as a likely major source (e.g. Floyd et al., 1998; Helvacı and Orti, 2004; García-Veigas and Helvacı, 2013). Various sized (several cm up to 7 m) and long (> 10 km) N-S oriented vertical or subvertical travertine veins are cutting epiclastic deposits in the north-western part of the caldera interior (Figs. 2, 5e, g, h).

## 3. Analytical techniques

### 3.1. Geochemistry

Rock powders of the selected fresh rock samples were prepared by removing the altered surfaces and powdered in a shatter box at Dokuz Eylül University. The geochemical data for 20 samples were performed by ACME Analytical Laboratories Ltd. in Vancouver (Table 1). Element abundances were determined by ICP–AES (major elements) and ICP–MS (trace elements), following a lithium-metaborate–tetraborate fusion and dilute nitric acid digestion of a 0.1 g sample. Weight loss on ignition (LOI) was determined by weight difference after ignition at 1000 °C. The precision for major elements was <1%. The precision for trace elements was in the order of 10%.

### 3.2. Ar–Ar methodology

$^{40}\text{Ar}/^{39}\text{Ar}$  geochronology was carried out on whole rock and biotite samples at the Auburn Noble Isotope Mass Analysis Laboratory (ANIMAL). The rock samples were selected after petrographic analysis from thin sections of each sample and then good candidates were chosen for dating. The selected samples were crushed and sieved for whole rock and biotite grains. The individual whole rock (250–212  $\mu\text{m}$ ) and biotite (850–600  $\mu\text{m}$ ) grains were hand-picked under the binocular microscope to be generally free from visible inclusion of other phases and free from visible alterations. The selected samples were washed with de-ionized water in an ultrasonic cleaner.

Samples were placed in an aluminum disk with an FC-2 monitor (age = 28.02 Ma, Renne et al., 1998) along with a  $\text{CaF}_2$  flux monitor. All samples and standards were irradiated in the USGS TRIGA reactor located at the Denver Federal Center, USA. ANIMAL is equipped with a low-volume, high sensitivity 10 cm radius sector mass spectrometer and automated sample extraction system (50 W Syndrad  $\text{CO}_2$  laser) for analysis of samples. The analyses of these samples were conducted

by laser incremental heating analysis (LIH) of approximately 100 grains of whole rock. The biotite samples were dated from single crystal total fusion (SCTF) and single crystal incremental heating (SCIH) methods. All statistical  $^{40}\text{Ar}/^{39}\text{Ar}$  ages in this study (weighted means, plateau, or isochron) are quoted at the standard deviation in precision of measurement, whereas errors in individual measurements are quoted at one standard deviation. Data reduction was calculated through the use of a customized Microsoft Excel application. The plateau and correlation ages were calculated by isoplot (Ludwig, 2003). A plateau in this study was defined as at least three or more contiguous increments containing >50% of the  $^{39}\text{ArK}$  in three or more contiguous steps with no resolvable slope among ages.

### 3.3. Sr–Nd isotopes

The  $^{87}\text{Sr}/^{86}\text{Sr}$  and  $^{143}\text{Nd}/^{144}\text{Nd}$  isotope analyses were performed on some of the samples analyzed in ACME Laboratories. The samples were not acid leached. The analyses were carried out at the Central Laboratory of the Middle East Technical University (METU, Ankara, Turkey). Analytical uncertainties are given at the  $2\sigma$  level.  $^{87}\text{Sr}/^{86}\text{Sr}$  data were normalized to  $^{86}\text{Sr}/^{88}\text{Sr}$  of 0.1194. During the course of the study, Sr standard NIST SRM 987 was measured as  $0.710247 \pm 10$  ( $n = 3$ ).  $^{143}\text{Nd}/^{144}\text{Nd}$  data were normalized to  $^{146}\text{Nd}/^{144}\text{Nd}$  of 0.7219. Measurement of the Nd La Jolla standard gave a value of  $0.511846 \pm 5$  ( $n = 3$ ). Age corrections have also been applied on the measured Sr and Nd isotopic ratios.

## 4. Petrochemistry and Sr–Nd isotope systematics

The TAS diagram (Fig. 7) defines a large compositional spectrum from mafic to felsic. On Harker diagrams of major elements (Fig. 8a), a liquid line of descent, evolving from basaltic-trachy-andesites (BTA) to trachy-andesites, trachy-dacites and Rhyolites-2, with increasing  $\text{SiO}_2$  is suggested. With few exceptions ( $\text{TiO}_2$  and  $\text{CaO}$ ) the basalts (full triangles) do not follow the discussed trend. The lamproites with  $\text{MgO} > 3\%$  and  $\text{K}_2\text{O}/\text{Na}_2\text{O} > 2$  even plotted in the basaltic-trachy-andesite field of TAS (Fig. 7) and show higher  $\text{TiO}_2$ ,  $\text{P}_2\text{O}_5$ ,  $\text{K}_2\text{O}$  and  $\text{MgO}$ , besides lower  $\text{Al}_2\text{O}_3$  and  $\text{Na}_2\text{O}$  in the Harker diagrams (Fig. 8a), defining a different kind of composition. Rhyolites (1 and 2) display a wider dispersion of  $\text{Na}_2\text{O}$  and  $\text{Al}_2\text{O}_3$ , as the sampling was of whole pyroclastic rocks (not only pumice) of which mineral/groundmass ratios are variable. The trace element Harker diagrams (Fig. 8b) mark a clear separation of Rhyolites-1 and Rhyolites-2. Rhyolites-2 have extremely low abundances of Ba, Sr, and  $\text{Eu}/\text{Eu}^*$ , a lower abundance of Zr and La and a much higher content in Nb, Y and Rb. By their higher values of Zr, La, Nb and Sr, the

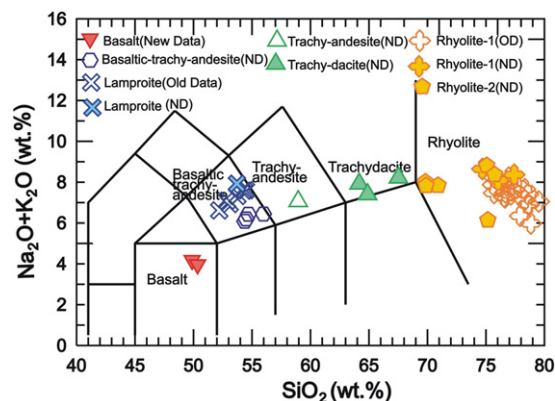


Fig. 7. Total alkali-silica (TAS) diagram for the studied rock samples, including the used symbols. The additional, published data on the diagram are from Floyd et al. (1998).

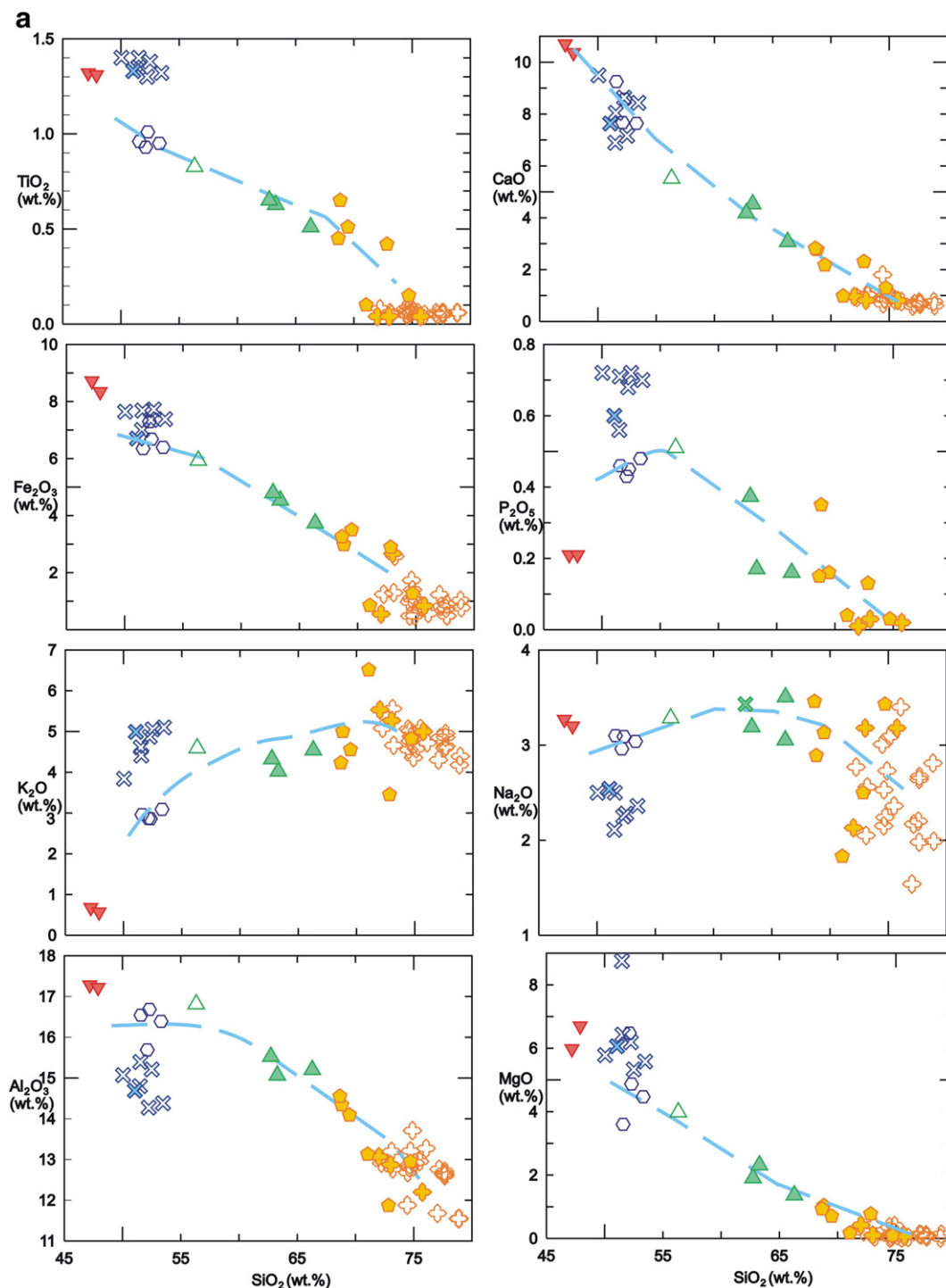
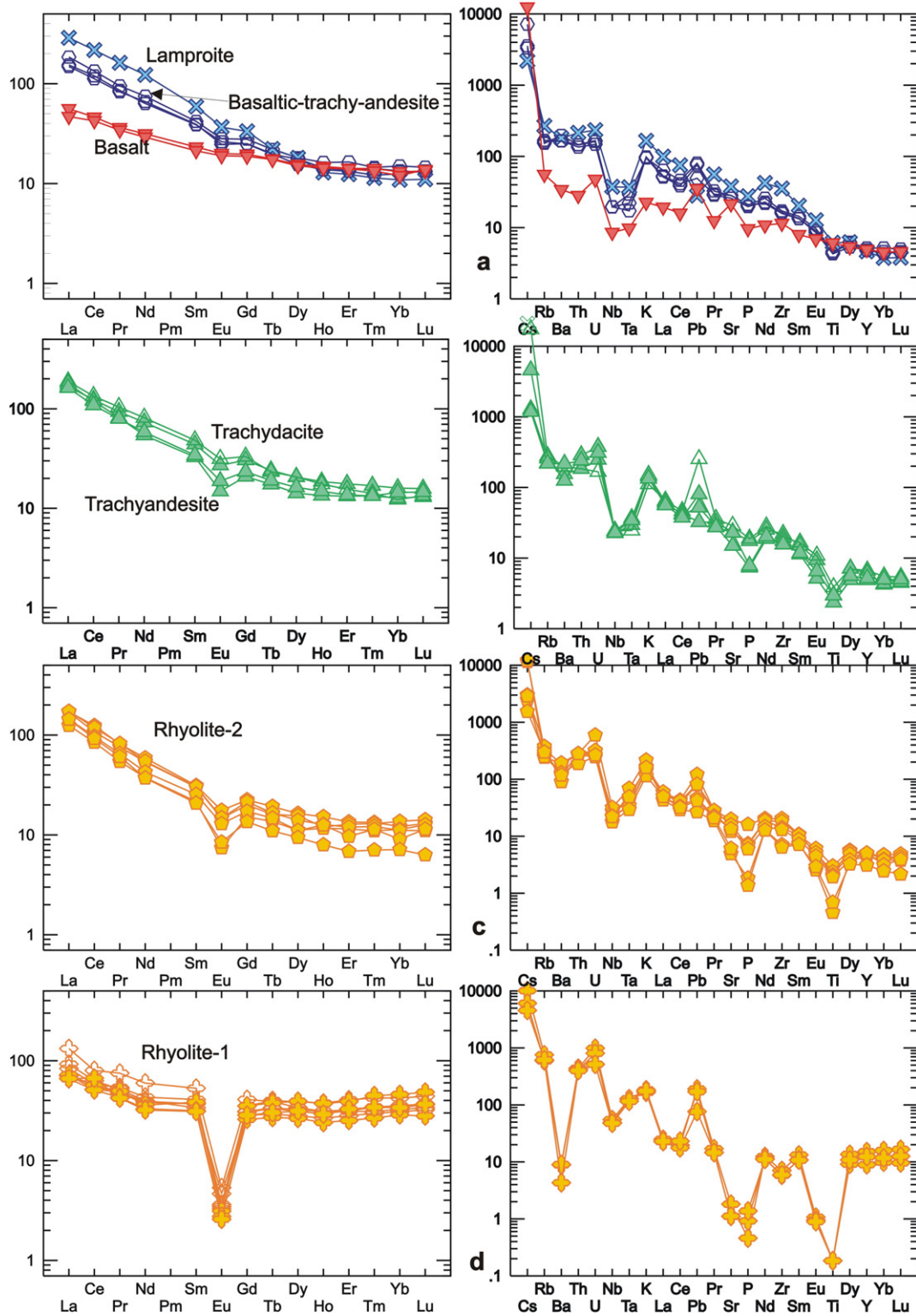


Fig.8. a. Harker diagram variations for major elements and; 8b. Harker diagram variations for minor elements and ratios. Symbols as in Fig. 6.

lamproites are also suggestive of a different source, however Rb, Y, V, Sc and  $\text{Eu}/\text{Eu}^*$  is similar with BTA. The low abundance of Ba, Nb and La of the basalts disagree, as in the case of major elements, with the primary composition of a liquid line of descent toward Rhyolites-2 that may be reasonably considered starting with BTA (Fig. 8b). Primitive mantle-normalized incompatible element patterns show negative anomalies for Nb-Ta, as well for P and Ti from more primitive to rhyolites and a positive Pb anomaly (Fig. 9a–d). The chondrite CI-normalized REE and primitive mantle patterns (Sun and McDonough, 1989) show that basalt (K1) is the most primitive and that there are small differences

between sample compositions starting from BTA to Rhyolite-2 showing a faintly increased Eu negative anomaly toward Rhyolites-2. Rhyolites-1 show a very different REE pattern with the highest Eu anomaly ( $\text{Eu}/\text{Eu}^* = 0.08\text{--}0.09$ ) and a flat “sea-gull” pattern of light and heavy REE, as well as very low Ba, Sr, P and Ti.

Thirteen Sr and Nd isotope analyses (Table 1) show the initial  $^{87}\text{Sr}/^{86}\text{Sr}$  and  $^{143}\text{Nd}/^{144}\text{Nd}$  ratios of the Kirka volcanics varying in large ranges, the most primitive for the basalts (0.7056–and 0.5127), then intermediate for the rest of the rocks, including lamproites, BTA and Rhyolite-2 (0.7065–0.7095 and 0.5124–0.5123) with exception of the Rhyolite-1



**Fig. 9.** CI – chondrite normalized REE and Primitive Mantle (PM)-normalized for studied samples: basalt, lamproite, basaltic-trachy-andesite; trachy-andesite and trachy-dacite; Rhyolite-2; Rhyolite-1. Normalizing factors are from Sun and McDonough (1989). Symbols as in Fig. 6.

that displays the highest values for  $^{87}\text{Sr}/^{86}\text{Sr}$  (0.7184–0.7210) and lower, but similar with Rhyolite-2 for  $^{143}\text{Nd}/^{144}\text{Nd}$  (0.5122–0.5123) (Fig. 10).

### 5. Ar-Ar geochronology

Published K-Ar dating on Rhyolite-1 ignimbrite on biotite yielded ages ranging from  $18.5 \pm 0.2$  to  $19.0 \pm 0.2$  (Helvacı, 1995; Savaşçın

and Oyman, 1998 and reference therein; Helvacı and Alonso, 2000). Three new Ar-Ar datings were performed on Rhyolite-2 ignimbrite, from the bottom of the caldera (K-6), from the eastern side (K50B) and a lava dome situated in the north (KG-91) (Table 2, Annex 1). The obtained time interval of  $18.58\text{--}18.83 \pm 0.07$  Ma suggests close,  $<0.2$  Ma eruption extents. The geological relationships implying that the ignimbrites of Rhyolite-2 closely followed Rhyolite-1

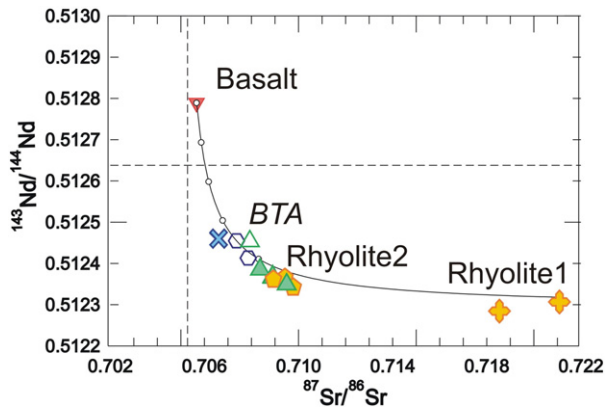


**Fig. 10.** Suggested mixing curve starting from the basalt (K1) in the Sr-Nd isotopic diagram for analyzed samples and ending to Rhyolite-1 (KG-111). Symbols as in Fig. 6.

ignimbrites are indicative of the manifold caldera collapse interval. In the error limit,  $18.83 \pm 0.07$  Ma for the Rhyolite-2 looks plausible for the end of caldera collapse events. The similar age obtained for the Rhyolite-2 domes (KG-91,  $18.72 \pm 0.04$ ) developed at the northern caldera margin, most probably the first post-caldera structures, which is in the same range. Ar-Ar ages of the trachyte rocks of the extra-caldera Kesenler volcano, are  $18.65\text{--}18.77 \pm 0.02$  Ma, ages which are a little bit younger than Rhyolites-1 and 2. Assuming that the post-caldera trachyte domes at the caldera border have similar ages, they also may have been generated a short time after collapse.

The  $18.63 \pm 0.22$  Ma age of the basalt found close to the base of the BMK-2009/1 borehole, intercalated or intruded in the ignimbrites (see Annex 1, Tables 2, 3 and Fig. 6), and signifies an eruption or intrusion in the existent inside-caldera sequence. Since the basalts did not reach the surface, it may be assumed that they were of small volume, most probably closely connected with the caldera collapse events.

The Ar-Ar ages (see Annex 1, Table 2) on post-caldera effusive BTA (16.92 Ma – K4) and the lamproites at Kesenler (16.21 Ma – 37B) suggest that such primitive volcanic products are the youngest and were generated after ~1 Myr. Such a situation where the calc-alkaline

rhyolites and associated products were followed by transitional high-Mg basaltic, trachytic and lamproitic compositions was already documented in north Anatolia, both related to the Eskişehir–Afyon volcanic area (EAV) and Menderes Massif core complex. This also suggests that primitive magmas can reach the surface at the same time with the rhyolitic ignimbrites or later (Akal et al., 2013; Aydar et al., 1998; Prelević et al., 2012; Ersoy and Palmer, 2013; Seghedi et al., 2013).

**6. Discussion**

*6.1. Volcanic evolution and caldera model*

The caldera initiation is a result of multiple explosive eruptions of Rhyolite-1 and Rhyolite-2 magmas (Fig. 2). Rhyolite-1 ignimbrites are extensively developed toward the south and are probably also present all around the northern edge, but this is only an assumption since they are covered by the Rhyolite-2 ignimbrites. The caldera shape is oval with a 24 km NNW-SSE long axis and a 15 km minor axis. The complete surrounding of the re-sedimented volcanoclastic deposits of the intracaldera facies along intercalated limestone deposition by the outflow ignimbrite and fall-out sheet typically constrain the position of the subsided block to be roughly within the limits of the outcropping intra-caldera facies. This subsided block was the location of isolated lake sedimentation developed up to its total filling. The transport directions of the re-sedimented volcanoclastic deposits, oriented toward the interior, define the caldera margins as the main source; the vast volume of ignimbrite and associated deposits were easily eroded and transported by streams or rivers to be re-deposited inside the caldera. The limestones represent a moment of tectonic calm that diminished the erosion and facilitated carbonate precipitation in the isolated caldera basin. Missing the short-distance correlation between the similar lithologies in the boreholes may suggest that the caldera bottom should be uneven and may be at ~1000–1200 m depth; however since not all the intra-caldera area was searched with boreholes, the whole subsidence arrangement is still uncertain. The dominant post-caldera magmas (BTA, trachy-andesites, trachy-dacites and lamproites) mainly caused the north and some east ring fault systems to erupt, generating effusive structures as lava domes or flows without causing resurgence (e.g., Kennedy et al., 2012). Therefore, the northern topographic border is almost completely hidden by the dome morphology of the younger post-caldera rocks and, as in many other calderas, suggests the location of its structural margin (Lipman, 2000; Cole et al., 2005).

The post-caldera eruptions of new magmas of a different origin drove further vigorous hydrothermal systems. The heat, volatiles and structural pathways provided by the hydrothermal fluids generated an initially large area of silica deposition and veining along ring fault structures, followed by borate deposition, and in the final stage by using the same N-S system of the deposition of large travertine deposits. Such active faulting clearly post-dated the collapse basin, since in the intra-caldera, various sediments (as terrigenous volcanoclastic and precipitated limestones) and pyroclastic deposits, observed in outcrops or suggested by the boreholes, are intensely ~N-S normally faulted (Fig. 5g, h). This hydrothermal system formed rapidly after the post-caldera events and was strongly enriched in magmatic volatiles and repositories for the borate deposition and perhaps for a long period was the source of geothermal energy. Such a post-caldera hydrothermal system is common for many of the calderas in the world (e.g., Cole et al., 2005; Kennedy et al., 2012). Possible mechanisms by which volcanism might supply B, S, Sr and Li to the caldera-basin sediments include the leaching of volcanic rocks by hot meteoric waters and post-caldera hydrothermal degassing (e.g. Helvacı and Alonso, 2000; García-Veigas and Helvacı, 2013).

*6.1.1. Volume estimation*

The intra-caldera basin form is elongated in a NW-SE direction showing a 24 km long axis × 15 km minor axis. If we assume that the depth might be about 800–1200 m, with an average of 900 m, in the

**Table 2**  
Succession of volcanic events based on the K-Ar (published) and Ar-Ar (new data) age determination in the Kirka-Phrigan caldera.

Events	Ages	References
<b>Post- or outside-caldera related</b>		
Lamproite (lava flows)	<b>16.21 ± 0.02 Ma</b> (37B, Kesenler volcano top)	<b>New data</b>
Basaltic-trachy-andesite (lava flows)	<b>16.92 ± 0.05 Ma</b> (K4, N caldera rim-Ildrisiyayla)	<b>New data</b>
Trachyte (pyroclastic or lava flows)	<b>18.65 ± 0.013 Ma</b> (37C, Kesenler volcano, upper); <b>18.77 ± 0.02 Ma (average)</b> ; <b>18.78 ± 0.05 Ma</b> (37A, Kesenler volcano, base)	<b>New data</b>
<b>End of caldera collapse events</b>		
Basalt (sill or lava) close to the caldera bottom	<b>18.63 ± 0.22 Ma</b> (K1, 955.8 m – BMK-2009/1)	<b>New data</b>
Rhyolite-2 (dome and ignimbrite)	<b>18.72 ± 0.04 Ma</b> (KG-91, average) <b>18.68 ± 0.04 Ma</b> (KG-91) <b>18.69 ± 0.04 Ma</b> (K6/1063 m – BMK-2009/1) <b>18.59 ± 0.05 Ma</b> ; <b>18.83 ± 0.07 Ma</b> (KG-50b, average)	<b>New data</b>
Rhyolite-1 (ignimbrite)	18.5 ± 0.2 – biotite (K/Ar)	Helvacı and Alonso (2000)
	19.0 ± 0.2 Ma – biotite (K-Ar)	Helvacı, 1995

**Table 3**  
Summary of  $^{40}\text{Ar}/^{39}\text{Ar}$  experiments.

Rock type	Sample	Analyzed	N	Total fusion		39Ar%	MSWD	Plateau		Average	
				Age(Ma)	$\pm 2\sigma$			Age(Ma)	$\pm 2\sigma$	Age(Ma)	$\pm 2\sigma$
Basalt	K1	wr	17 to23	19.80	$\pm 1.3$	57.1	0.85	18.63	$\pm 0.22$		
Rhyolite-2	K6	BiotitePP	18			95.0	0.69			18.69	$\pm 0.02$
Rhyolite-2	K6	BiotitelH	10 to17	18.70	$\pm 0.13$	95.1	1.7	18.69	$\pm 0.04$		
Rhyolite-2	KG-50b	K-feldspar	10			95.0	1.4			18.83	$\pm 0.07$
Rhyolite-2	KG-50b	K-feldspar	11			100	0.96	18.59	$\pm 0.05$		
Rhyolite-2	KG-91	K-feldspar	16			100.0	1.11	18.65	$\pm 0.02$		
Rhyolite-2	KG-91	Biotite	17			95.0	0.65			18.72	$\pm 0.04$
Rhyolite-2	KG-91	Biotite	13			99.3	1.8	18.68	$\pm 0.043$		
Rhyolite-2	KG-91	Biotite	14			99.2	0.76	18.58	$\pm 0.05$		
TD	KG-37 A	Biotite	16			95.0	1.3			18.77	$\pm 0.02$
TD	KG-37 A	Biotite	9			95.7	0.19	18.78	$\pm 0.05$		
TD	KG-37C	Plagioclase	2 to 17			100.0	1.6	18.65	$\pm 0.013$		
BTA	K4	wr	10 to 18	17.06	$\pm 0.17$	69.9	1.2	16.92	$\pm 0.05$		
Lamproite	KG-37B	wr	1 to 19	16.28	$\pm 0.08$	100.0	5.4				
Lamproite	KG-37B	wr	11 to 19			67.6	0.90	16.21	$\pm 0.02$		

Abbreviations: TD – trachy-dacite; BTA – basaltic-trachy-andesite; N – number of steps; wr – whole rock; MSWD – mean squares of weighted deviates.

case of a piston-like collapse and assuming the shape of the caldera to be roughly cylindrical, we might have an area of collapse with a volume of  $\sim 30 \text{ km}^3$ . Taking into account the specific gravity of tuffs and lavas of  $\sim 2.2 \text{ kg/m}^3$ , it results around  $60\text{--}70 \times 10^9$  tons of materials that flared up from the magma chamber during caldera generation.

6.2. Petrogenetic model

6.2.1. Fractional crystallization and crustal assimilation

$\text{SiO}_2$ -variation diagrams define trends that are consistent with liquid lines of descent between BTA and Rhyolite-2 (Fig. 8a, b). The Harker trends indicate fractional crystallization of olivine, clinopyroxene and Fe-Ti oxides, followed by plagioclase crystallization. The most primitive basalt (K1) is less evolved with the highest MgO ( $\sim 6.0 \text{ wt.}\%$ ) and may be a potential source for the BTA. Extreme depletion of Sr, Eu, and Ba and elevated Rb/Sr of Rhyolite-1 compared with Rhyolite 2, also associated with high isotopic initial Sr ratio, suggest a different evolution and source, most probably a crustal one, to be either granodiorite or silica-rich plutons that lack titanite (Glazner et al., 2008). According to Bachmann and Bergantz (2008a) this is an exceptional situation with the presence of both cool and wet magma (Rhyolite-1 resulting from crustal partial melting) assumed for hotspot systems and continental rifts, and hot and dry magma (Rhyolite-2 resulting from fractional crystallization), attributed to convergent margin systems.

In order to test the fractional crystallization and assimilation processes, we adopted the DePaolo (1981) model using IgPet software (Carr, 2010). The bulk-partition coefficients were estimated from phase proportions of the fractionated assemblages, and considering the wall rock assimilation

rate (Ma, mass/unit time) and fractionation rate (Mc, mass/unit time) and by varying the assimilation/fractionation rate ( $R = \text{Ma}/\text{Mc}$ ) from 0 to 1. AFC model results have to accomplish the  $^{143}\text{Nd}/^{144}\text{Nd}$ ,  $^{87}\text{Sr}/^{86}\text{Sr}$ , Nd and Sr constraints of the final products (Fig. 11).

Firstly the  $^{87}\text{Sr}/^{86}\text{Sr}$  vs. Sr and  $^{143}\text{Nd}/^{144}\text{Nd}$  vs. Nd evolution was modeled assuming K1 basalt as the endmember for the BTA (Fig. 11). It appears that low  $D_{\text{Sr}}$  (0.4) and  $D_{\text{Nd}}$  (0.45) values reasonably satisfy the AFC model using local crustal composition (Okay and Satır, 2006) for  $R = 0.4$ . This is in agreement with dominant fractionation of pyroxene and olivine and less of plagioclase with a liquid fraction  $F = \text{Mm}_{(\text{magma mass})}/\text{Mmi}_{(\text{initial magma mass})}$  of  $\sim 0.5\text{--}0.7$  for such composition. In the same diagram we applied modeling from BTA (K94) to trachy-andesite to Rhyolite-2. This can be satisfied considering  $R = 1$  that implies  $F = \text{Ma}/\text{Mm}$  of  $\sim 0.4$  with higher  $D_{\text{Sr}}$  (2) and  $D_{\text{Nd}}$  (2.5). Plagioclase became an important fractionation phase as revealed by the negative Eu anomalies relative to chondrites. Rhyolite-1 magma is not a result of AFC showing very high isotopic values of  $^{87}\text{Sr}/^{86}\text{Sr}$  vs. Sr, close to the local crustal ones and proposing crustal anatexis. In the  $^{143}\text{Nd}/^{144}\text{Nd}$  vs. Nd modeling, Rhyolite-1 is in the extension of the BTA-AFC modeling, at higher F, suggesting a possible mixing trend with an anatectic source. In both cases the lamproite shows a different behavior.

6.2.2. Source characteristics of the magmas

There are two main magma sources in Kirka, one is typical, but heterogeneous mantle-derived and the other is crustal, represented by the Rhyolites-1 with their distinctive “sea gull” shape REE pattern (Glazner et al., 2008). The most primitive basalts show an undersaturated Na-alkaline character on the  $\text{K}_2\text{O}/\text{Na}_2\text{O}$  vs.  $\Delta\text{Q}$  diagram (Fig. 12a). Toward the east

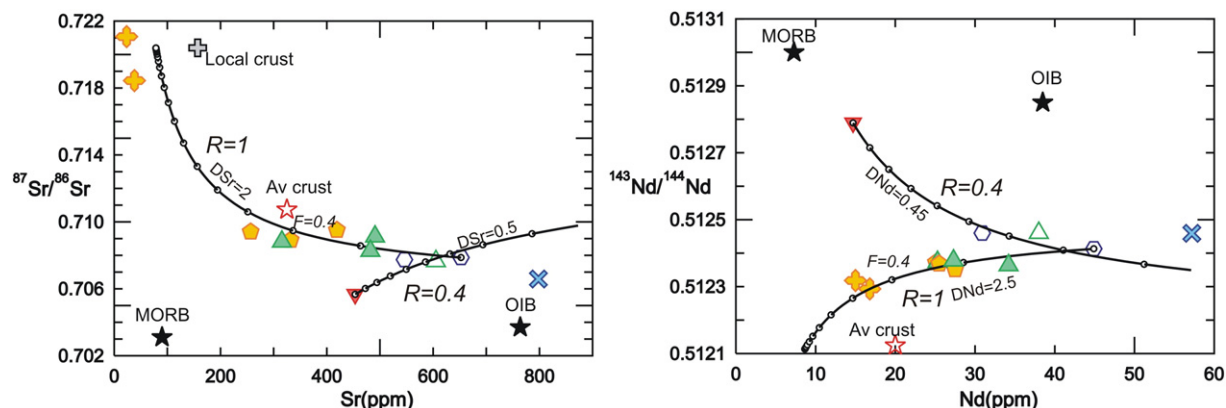
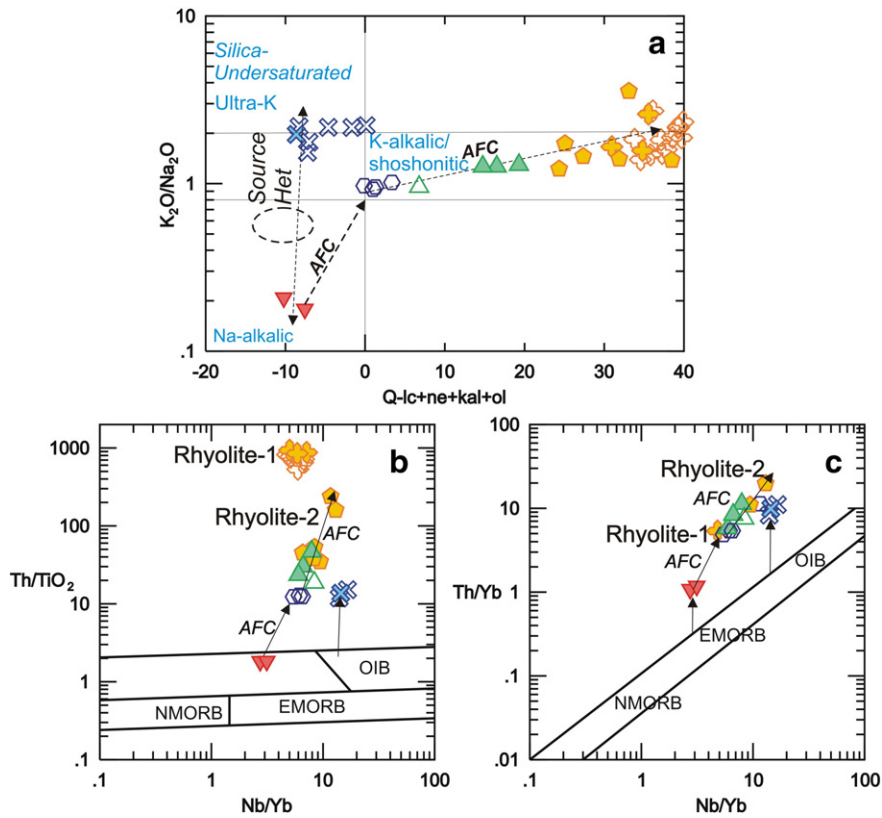


Fig. 11.  $^{87}\text{Sr}/^{86}\text{Sr}$  vs. Sr and  $^{143}\text{Nd}/^{144}\text{Nd}$  vs. Nd evolution and modeling using Carr's (2010) software. Symbols as in Fig. 6.



**Fig. 12.** a. The silica saturation index  $\Delta Q = Q - [lc + ne + kal + ol]$  was calculated using CIPW norm vs.  $K_2O/Na_2O$  diagram (according to Peccerillo, 2002); b, c –  $TiO_2/Yb$  vs.  $Nb/Yb$  and the  $Th/Yb$  and  $Nb/Yb$  ratios (according to Pearce, 2008).

of Kirka in the Tunçbilek–Domanıç basin, the Karaköy basalts show similar characteristics (Ersoy and Helvacı, 2016; Helvacı et al., 2016) and those associated with Menderes Massif were interpreted as transitional basalts (Ersoy et al., 2008; Seghedi et al., 2013). The younger lamproites represent the other mantle-derived mafic rocks in the region, suggesting

significant mantle heterogeneities. In both diagrams, a two step AFC starting with basalts is inferred from the modeling. Original mantle composition and inferred subduction-related geochemical enrichment process of the most primitive rocks in Kirka can be approximated by using  $TiO_2/Yb$  vs.  $Nb/Yb$  and  $Th/Yb$  and  $Nb/Yb$  ratios (Fig. 12b, c; Pearce,

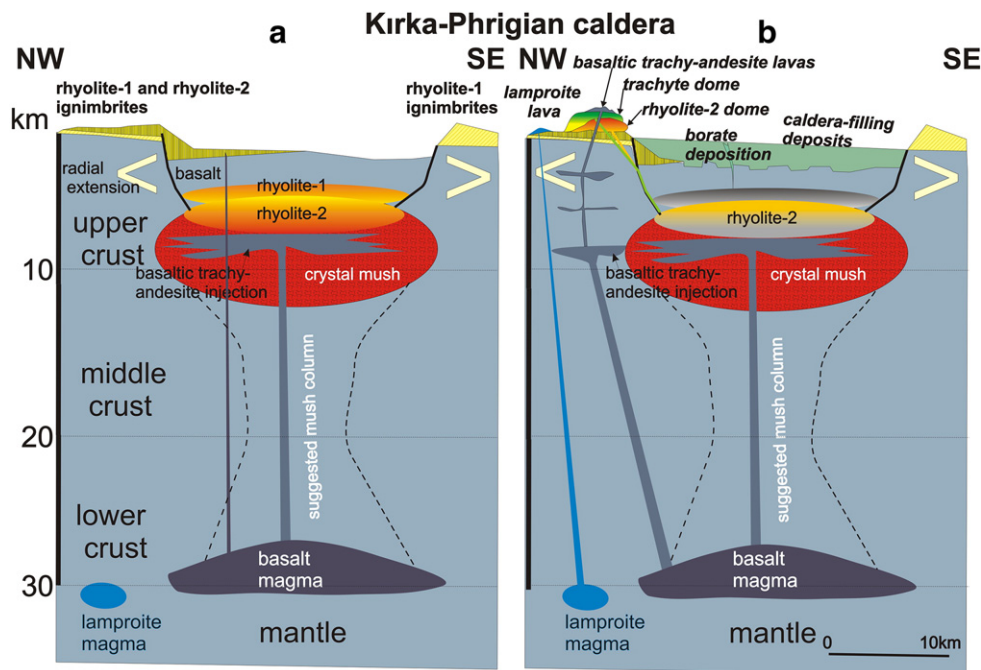


**Fig. 13.** Hypothesized magmatic system evolution of the Kirka-Phrigan caldera. The model is adapted from Hildreth (2004) and Bachmann and Bergantz (2008a,b); a. caldera collapse processes including the generation of Rhyolite-1 and 2 ignimbrites; b. post-caldera filling processes, lava dome and lava formation at the northern edge (rhyolites, trachytes shortly after the collapse), and then basaltic-trachy-andesites and lamproites (at ~2 Myr after the collapse).

2008). The basalts plot close to the *E*-MORB field and the lamproites closer to OIB, indicating that their mantle source below Kirka is heterogeneous and variably enriched. Subduction-related geochemical enrichment process are best monitored by Th/Yb ratio which is slightly enriched with respect to the mantle array, indicating a reduced amount of subduction-derived material in the most primitive basalt genesis. It is already recognized that the Miocene volcanic rocks in western Anatolia were derived from enriched mantle sources influenced by subduction-related metasomatism (Aldanmaz et al., 2000; Yilmaz et al., 2001; Innocenti et al., 2005; Prelević et al., 2012; Ersoy and Palmer, 2013).

### 6.3. Evolutionary model

The combined petrographical, geochemical, chronological and lithofacies characteristics based on the data obtained in the caldera interior, and to a lesser extent in the exterior, was used to define the evolutionary model (Fig. 13a,b). The absence of observations from the outside northern and southern regions of the caldera obtained only from the existing geological maps, including a lack of correlation in lithofacies analyses make it difficult however, to understand the whole system. We consider the following evolutionary model as a working hypothesis and further and more detailed study may confirm, disprove or enhance the knowledge we were able to assemble up to now.

#### 6.3.1. Pre-caldera magmatic system

Many recent studies have recognized the predominance of mushy, crystal-rich systems in controlling the physical and chemical evolution of crustal felsic reservoirs (e.g., Bachmann and Bergantz, 2004, 2008b; Dufek and Bachmann, 2010; Cashman and Blundy, 2013; Caricchi and Blundy, 2016). During the prolonged volcanic activity, the high dimension crystal mush-type magma chamber enclosed variable amounts of interstitial melt, with localized shallow levels of bodies of eruptible ignimbrite magma beneath upcoming caldera generation (Lipman and Bachmann, 2015; Geyer and Marti, 2014) (Fig. 13a).

During the temporal evolution of the chemistry and physical properties of Kirka-Phrigian magmatic systems we may infer that the existence of two different rhyolite compositions (1st anatectic and 2nd as result of crystal fractionation) and their sequential eruption (2nd after the 1st) suggests a long time residence of a magmatic system that allowed differentiation processes of a *BTA*-type magma with generation of a liquid that increased the temperature and started the anatexis of highly fertile crust material (garnet-bearing as indicated by numerous such xenocrysts found in Rhyolite-1). As the magma corresponding to the Rhyolite-1 was initially extracted, it should start from the top of the melt lenses and then propagate downward to withdraw the Rhyolite-2 magma. We may agree that the anatectic melt was in the upper part of the system, as a part of a complex magma reservoir (e.g., Cashman and Giordano, 2014).

#### 6.3.2. Caldera eruption processes

Repeated generation of rhyolite magma starting at the top of vertically extensive bodies of a crystal mush in the upper crust, initially underlain by voluminous input from mafic mantle-derived magma (*BTA*) and a new more primitive one (Basalt), led to repeated ignimbrite eruptions and caldera formation in the Kirka-Phrigian caldera. The initial eruption was discharged in the south of the system with Rhyolites-1 ignimbrites that shows a rapid agglutination, welding and rheomorphism, and besides a high discharge rate and a short time of emplacement, in accordance with experimental data (Lavallée et al., 2015). Such a situation also suggests that, in most cases, heat loss was insignificant during flow emplacement and characteristic for an en-mass low-eruptive column (e.g., Sommer et al., 2013; Wolff and Wright, 1981).

The second major collapse event was related to the Rhyolites-2 and mostly discharged as Plinian eruption columns (e.g., the association of pyroclastic flows with thick fall-out deposits) deposited toward the north, generating intra- and extra-caldera ignimbrites. This implies a

vent migration toward the north along the caldera fault system causing major instabilities for the roof system. It is obvious that the southern margin (dominated by welded Rhyolite-1 ignimbrites) and the northern one (dominated by non-welded Rhyolite-2 ignimbrites and post-caldera structures) did not behave similarly after each major collapse event and vent migration, meaning that the calderas's fault system at the northern part remained active for a longer time than the southern one that may have been sealed after the initial collapse of the Rhyolite-1 ignimbrite eruption. Although there is no direct way to say if the caldera floor after the collapse was a symmetrical (piston-like) or asymmetrical (trap-door-like) block, or multiple smaller blocks (piecemeal type), for the moment, the general suggestion, supported by the borehole cores go to the last mentioned alternative. The latest stage generation of a thick deposit of fall-out tuffs with accretionary lapilli suggests that the eruption was triggered by magma-water interaction. The water had most probably accumulated in the early collapse basin and reworked filling deposits of the Kirka-Phrigian caldera. The north-easternmost rhyolite dome system at the circular northern rim, surrounded by a hyalo-breccia envelope, also suggests a subaqueous domain during emplacement and hyaloclastic fragmentation.

## 7. Conclusions

Several eruption events initiated a complex collapse system at ~18.9 Ma and a large roughly elliptical (24 km × 15 km) caldera, ~900–1000 m depth with extra-caldera outflow ignimbrites, dominantly Rhyolite-1 toward the south and Rhyolite-2 toward the north. Vent migration toward the north is suggested. The intrusion of basalts (~18.63 ± 0.22 Ma) at the base of the caldera may be responsible for triggering some of the caldera eruptions and collapse events.

The effusive eruptive event (18.7–18.63 Ma), generating rhyolite and trachyte domes at the northern caldera edge, was closely associated with caldera-filling processes dominated by volcanoclastic deposits and Middle Miocene limestone precipitation. The youngest volcanic events (16.92–16.21 Ma) are represented by the effusive lavas of *BTA* (basaltic-trachy-andesites) and lamproites.

Post-volcanic activity – following NNW-SSE faulting was dominated by hydrothermal activity with world-class borate and travertine deposition. The final geological event was related to important erosional processes toward the east, followed by regional Late Miocene limestone precipitation that extended all over inside and outside of the eastern caldera.

Initial ignimbrite eruptions (Rhyolites-1) suggest a crustal origin; the next ignimbrite eruptions (Rhyolites-2) along with trachytes were the result of two step differentiation of *BTA* that is considered to be a differentiated product of unsaturated basalts ponding at the base of the crust (Fig. 13). A shift to small volume episodic basaltic, trachytic and lamproitic volcanism indicates two types of primitive magma input which had an origin in a variably enriched mantle lithosphere. The petrogenetic observations and an inferred extensional setting favored multiple magma sources associated with caldera-related volcanism; however the precursory extensional tectonic processes anticipating the caldera generation are so far not understood.

Supplementary data to this article can be found online at <http://dx.doi.org/10.1016/j.jvolgeores.2016.09.007>.

## Acknowledgements

This work was supported by the Dokuz Eylül University Scientific Project (Bilimsel Araştırma Projesi) No: 2010.KB.FEN.009. We thank Selman Aydoğan and Berk Çakmakçoğlu for their drafting assistance. We recognize the assistance of Yasin Aydın during the field study and Yeşim Yücel Öztürk during logging. We thank Yalçın Ersoy for his advices. We also thank the ETİBANK Mine Company General Management for their logistic support during the field study and for their permission to publish the simplified lithology of the borehole data. We are grateful to Hilary Downes for English corrections. A grant of the Ministry of

National Education, Romania, project number PN-II-ID-PCE-2012-4-0137 is acknowledged. Constructive comments provided by Adelina Geyer and Cüneyt Şen helped us to improve the initial manuscript. Thorough editorial handling by Heidi M. Mader is appreciated.

## References

- Akal, C., Helvacı, C., Prelević, D., van den Bogaard, P., 2013. High-K volcanism in the Afyon region, western Turkey: from Si-oversaturated to Si-undersaturated volcanism. *Int. J. Earth Sci.* 102, 435–453.
- Aldanmaz, E., Pearce, J.A., Thirlwall, M.F., Mitchell, J.G., 2000. Petrogenetic evolution of late Cenozoic, post-collision volcanism in western Anatolia Turkey. *J. Volcanol. Geotherm. Res.* 102, 67–95.
- Ayder, E., Bayhan, H., Gourgaud, A., 1998. Köroğlu caldera, mid-west Anatolia, Turkey: volcanological and magmatological evolution. *J. Volcanol. Geotherm. Res.* 85, 83–98.
- Bachmann, O., Bergantz, G.W., 2004. On the origin of crystal-poor rhyolites: extracted from batholithic crystal mushes. *J. Petrol.* 45, 1565–1582. <http://dx.doi.org/10.1093/ptrology/egh019>.
- Bachmann, O., Bergantz, G.W., 2008a. Rhyolites and their source mushes across tectonic settings. *J. Petrol.* 49, 2277–2285. <http://dx.doi.org/10.1093/ptrology/egn068>.
- Bachmann, O., Bergantz, G.W., 2008b. The magma reservoirs that feed supereruptions. *Elements* 4, 17–21.
- Caricchi, L., Blundy, J., 2016. The temporal evolution of chemical and physical properties of magmatic systems. In: Caricchi, L., Blundy, J.D. (Eds.), *Chemical, Physical and Temporal Evolution of Magmatic Systems*. Geological Society, London, Special Publications, p. 422 <http://dx.doi.org/10.1144/SP422.11>.
- Carr, M., 2010. IGPEP. Software Program. Terra Softa Inc., 155 Emerson RD., Somerset, NJ 08873.
- Cashman, K., Blundy, J., 2013. Petrological cannibalism: the chemical and textural consequences of incremental magma body growth. *Contrib. Mineral. Petrol.* 166 (3), 703–729.
- Cashman, K.V., Giordano, G., 2014. Calderas and magma reservoirs. *J. Volcanol. Geotherm. Res.* 288, 28–45.
- Cole, J.W., Milner, D.M., Spinks, K.D., 2005. Calderas and caldera structures: a review. *Earth Sci. Rev.* 69, 1–26.
- DePaolo, D.J., 1981. Trace element and isotopic effects of combined wallrock assimilation and fractional crystallization. *Earth Planet. Sci. Lett.* 53, 189–202.
- Dilek, Y., Altunkaynak, Ş., 2009. Geochemical and temporal evolution of Cenozoic magmatism in western Turkey: mantle response to collision, slab break-off, and lithospheric tearing in an orogenic belt. In: van Hinsbergen, D.J.J., Edwards, M.A., Govers, R. (Eds.), *Collision and Collapse at the Africa–Arabia–Eurasia Subduction Zone*. Geological Society, London, Special Publications 311, pp. 213–233.
- Dilek, Y., Altunkaynak, Ş., 2010. Geochemistry of Neogene–Quaternary alkaline volcanism on western Anatolia, Turkey, and implications for the Aegean mantle. *Int. Geol. Rev.* 52, 631–655.
- Dufek, J., Bachmann, O., 2010. Quantum magmatism magmatic compositional gaps generated by melt–crystal dynamics. *Geology* 38 (8), 687–690.
- Ersay, E.Y., Helvacı, C., 2016. Geochemistry and petrology of the lower Miocene bimodal volcanic units in the Tunçbilek–Domañic basin, western Anatolia. *Int. Geol. Rev.* <http://dx.doi.org/10.1080/00206814.2016.1147385>.
- Ersay, E.Y., Palmer, M.R., 2013. Eocene–Quaternary magmatic activity in the Aegean: implications for mantle metasomatism and magma genesis in an evolving orogeny. *Lithos* 180–181, 5–24.
- Ersay, E.Y., Helvacı, C., Sözbilir, H., Erkül, F., Bozkurt, E., 2008. A geochemical approach to Neogene–Quaternary volcanic activity of western Anatolia: an example of episodic bimodal volcanism within the Selendi Basin, Turkey. *Chem. Geol.* 255, 265–282.
- Floyd, P.A., Helvacı, C., Mittweide, S.K., 1998. Geochemical discrimination of volcanic rocks associated with borate deposits: an exploration tool? *J. Geochem. Explor.* 60 (185–20).
- Freundt, A., Wilson, C.J.N., Carey, S.N., 2000. Ignimbrites and block-and-ash flow deposits. In: Sigurdsson, H. (Ed.), *Encyclopedia of Volcanoes*. Academic Press, San Francisco, pp. 581–601.
- García-Veigas, J., Helvacı, C., 2013. Mineralogy and sedimentology of the Miocene Göcenoluk borate deposit, Kirka district, western Anatolia, Turkey. *Sediment. Geol.* 290, 85–96.
- Geyer, A., Martí, J., 2014. A short review of our current understanding of the development of ring faults during collapse caldera formation. *Front. Earth Sci.* 2, 22. <http://dx.doi.org/10.3389/feart.2014.00022>.
- Glazner, A.F., Coleman, D.S., Bartley, J.M., 2008. The tenuous connection between high-silica rhyolites and granodiorite plutons. *Geology* 36, 1047–1050.
- Gök, S., Çakır, A., Dündar, A., 1980. Stratigraphy, petrography and tectonics of the borate-bearing Neogene in the vicinity of Kirka. *Bull. Geol. Congr. Turk.* 2, 53–62.
- Göncüoğlu, C.M., Özcan, A., Turhan, N., Işık, A., 1992. Stratigraphy of the Kütahya region. A Geotraverse Across Tethyan Suture Zones in NW Anatolia. Field Guide Book for the Symposium on the Geology of the Black Sea Region, Ankara, pp. 3–11.
- Helvacı, C., 1977. *Geology, Mineralogy, and Geochemistry of the Borate Deposits and Associated Rocks at the Emet Valley, Turkey* (Ph.D. Thesis) University of Nottingham, UK, p. 338.
- Helvacı, C., 1995. Stratigraphy, mineralogy, and genesis of the Bigadiç borate deposits, Western Turkey. *Econ. Geol.* 90, 1237–1260.
- Helvacı, C., 2005. Borates. In: Shelley, R.C., Cocks, L.R.M., Plimer, I.R. (Eds.), *Encyclopedia of Geology* vol. 3. Elsevier, pp. 510–522.
- Helvacı, C., Alonso, R.N., 2000. Borate deposits of Turkey and Argentina: a summary and geological comparison. *Turk. J. Earth Sci.* 9, 1–27.
- Helvacı, C., Ortı, F., 2004. Zoning in the Kirka borate deposit, western Turkey: primary evaporitic fractionation or diagenetic modifications? *Can. Mineral.* 42 (4), 1179–1204.
- Helvacı, C., Ortı, F., García-Veigas, J., Rosell, L., Gündoğan, I., Yücel-Öztürk, Y., 2012. Neogene borate deposits; a workshop with special emphasis on the Anatolian deposits. In: Helvacı, C. (Ed.), *International Earth Science Colloquium on the Aegean Region, IESCA 2012, Workshop Book*, p. 64.
- Helvacı, C., Ersoy, E.Y., Billor, Z., 2016. Stratigraphy and Ar/Ar geochronology of the Miocene lignite-bearing Tunçbilek–Domañic Basin, western Anatolia. *Int. J. Earth Sci. (Geol. Rundsch)* <http://dx.doi.org/10.1007/s00531-016-1386-0>.
- Hildreth, W., 2004. Volcanological perspectives on Long Valley, Mammoth Mountain, and mono craters: several contiguous but discrete systems. *J. Volcanol. Geotherm. Res.* 136, 169–198. <http://dx.doi.org/10.1016/j.jvolgeores.2004.05.019>.
- İnan, K., Dunham, A.C., Esson, J., 1973. Mineralogy, chemistry and origin of Kirka borate deposit, Eskişehir Province, Turkey. *Trans. Inst. Min. Metall.* 82B, 114–123.
- Innocenti, F., Agostini, S., Di Vincenzo, G., Doglioni, C., Manetti, P., Savaşçın, M.Y., Tonarini, S., 2005. Neogene and Quaternary volcanism in Western Anatolia: magma sources and geodynamic evolution. *Mar. Geol.* 221, 397–421.
- Keller, J., Villari, L., 1972. Rhyolitic ignimbrites in the region of Afyon (Central Anatolia). *Bull. Volcanol.* 36, 342–358.
- Kennedy, B., Wilcock, J., Stix, J., 2012. Caldera resurgence during magma replenishment and rejuvenation at Valles and Lake City calderas. *Bull. Volcanol.* 74, 1833–1847.
- Kissel, C., Laj, C., Poisson, A., Görür, N., 2003. Paleomagnetic reconstruction of the Cenozoic evolution of the Eastern Mediterranean. *Tectonophysics* 362, 199–217.
- Kistler, R.B., Helvacı, C., 1994. Boron and borates. In: Carr, D.D. (Ed.), *Industrial Minerals and Rocks*, 6th ed. Soc. Min. Metallurgy and Exploration, Inc., pp. 171–186.
- Koçyiğit, A., 2005. The Denizli graben-horst system and the eastern limit of western Anatolian continental extension: basin fill, structure, deformational mode, throw amount and episodic evolutionary history, SW Turkey. *Geodin. Acta* 18 (3–4), 167–208.
- Lavallée, Y., Dingwell, D.B., Johnson, J.B., Cimarelli, C., Hornby, A.J., Kendrick, J.E., von Aulock, F.W., Kennedy, B.M., Andrews, B.J., Wadsworth, F.B., Rhodes, E., Chigna, G., 2015. Thermal vesiculation during volcanic eruptions. *Nature* 528, 544–547.
- Lefevre, C., Bellon, H., Poisson, A., 1983. Occurrence of leucitites among the Pliocene volcanics of Isparta (western Taurides, Turkey). *C. R. Acad. Sci. II* 297, 367–372.
- Lipman, P.W., 2000. Calderas. In: Sigurdsson, H. (Ed.), *Encyclopedia of Volcanoes*. Academic Press, San Francisco, pp. 643–662.
- Lipman, P.W., Bachmann, O., 2015. Ignimbrites to batholiths: integrating perspectives from geological, geophysical, and geochronological data. *Geosphere* 11 (3), 705–743. <http://dx.doi.org/10.1130/GES01091.1>.
- Ludwig, K.R., 2003. User's manual for Isoplot, v. 3.0, a geochronological tool kit for Microsoft Excel. Berkeley Geochronological Center, Berkeley, CA, Special Publication No. 4.
- McLane, M., 1995. *Sedimentology*. Oxford University Press, New York (423pp.).
- Okay, A.I., 2011. Taşanlı zone: the northern subducted margin of the Anatolide-Tauride block. *Miner. Res. Explor. Bull.* 142, 191–221.
- Okay, A.I., Satır, M., 2006. Geochronology of Eocene plutonism and metamorphism in northeast Turkey: evidence for a possible magmatic arc. *Geodin. Acta* 19 (5), 251–266.
- Okay, A.I., Harris, N.B.W., Kellay, S.P., 1998. Exhumation of blueschists along a Tethyan suture in northwest Turkey. *Tectonophysics* 285, 275–299.
- Özcan, A., Göncüoğlu, M.C., Turan, N., Uysal, Ş., Şentürk, K., Işık, A., 1988. Late Paleozoic evolution of the Kütahya–Bolkardağ belt. Middle East Technical University. *J. Pure Appl. Sci.* 21, 211–220.
- Pearce, J.A., 2008. Geochemical fingerprinting of oceanic basalts with applications to ophiolite classification and the search for Archean oceanic crust. *Lithos* 100 (1), 14–48.
- Peccerillo, A., 2002. Quaternary magmatism in Central–Southern Italy: a new classification scheme for volcanic provinces and its geodynamic implications. *Boll. Soc. Geol. Ital.* 1, 113–127.
- Prelević, D., Akal, C., Foley, S.F., Romer, R.L., Stracke, A., Van Den Bogaard, P., 2012. Ultrapotassic mafic rocks as geochemical proxies for post-collisional dynamics of orogenic lithospheric mantle: the case of southwestern Anatolia, Turkey. *J. Petrol.* 53, 1019–1055.
- Prelević, D., Akal, C., Romer, R.L., Mertz-Kraus, R., Helvacı, C., 2015. Magmatic response to slab tearing: constraints from the Afyon Alkaline Volcanic Complex, Western Turkey. *J. Petrol.* 1, 36. <http://dx.doi.org/10.1093/ptrology/egv008>.
- Renne, P.R., Swisher, C.C., Deino, A.L., Karner, D.B., Owens, T.L., DePaolo, D.J., 1998. Inter-calibration of standards, absolute ages, and uncertainties in <sup>40</sup>Ar/<sup>39</sup>Ar dating. *Chem. Geol.* 145, 117152.
- Savaşçın, M.Y., Oyman, T., 1998. Tectono-magmatic evolution of alkaline volcanics at the Kirka–Afyon–Isparta structural trend, SW Turkey. *Tr. J. Earth Sci.* 7, 201–214.
- Seghedi, I., Ersoy, Y.E., Helvacı, C., 2013. Miocene–Quaternary volcanism and geodynamic evolution in the Pannonian Basin and the Menderes Massif: a comparative study. *Lithos* 180–181, 25–42.
- Sommer, C.A., Lima, E.F., Machado, A., Rossetti, L., de Magalhães, M., Pierosan, R., 2013. Recognition and characterization of high-grade ignimbrites from the Neoproterozoic rhyolitic volcanism in southernmost Brazil. *J. S. Am. Earth Sci.* 47, 152–165.
- Sun, S.-S., McDonough, W.F., 1989. Chemical and isotopic systematics of oceanic basalts: implications for mantle composition and processes. *Geol. Soc. Lond., Spec. Publ.* 42, 313–345.
- van Hinsbergen, D.J.J., Schmid, S.M., 2012. Map view restoration of Aegean–West Anatolian accretion and extension since the Eocene. *Tectonics* 31, TC5005. <http://dx.doi.org/10.1029/2012TC003132>.
- Wolff, J.A., Wright, J.V., 1981. Rheomorphism of welded tuffs. *J. Volcanol. Geotherm. Res.* 10, 13–34.
- Yağmurlu, F., Savaşçın, Y., Ergün, M., 1997. Relation of alkaline volcanism and active tectonism within the evolution of Isparta Angle, SW-Turkey. *J. Geol.* 105, 717–728.
- Yılmaz, Y., Genç, S.C., Karacık, Z., Altunkaynak, S., 2001. Two contrasting magmatic associations of NW Anatolia and their tectonic significance. *J. Geodyn.* 31, 243–271.